Anonymous Referee #1

General comments:

- *The authors have done an impressively thorough job of responding to the concerns raised by both reviewers. They have satisfied all of the major and minor concerns that I had about the manuscript. (This type of response is one of the most rewarding aspects of being a reviewer, in my opinion.)*
With these changes, the revised manuscript would be an excellent contribution to GMD; I therefore recommend that it be published pending a couple minor grammatical/syntactical issues noted below.

We thank the reviewer for the detailed reviewing. The text has been revised as the reviewer suggested.

Specific comments:

- *line 136: "precipitation event" -> "precipitation events"*

Corrected.

- *lines 144-145: I'd suggest revising the end of the sentence to "...were caused by wind shear associated with the Meiyu front in recent decades"*

Revised.

Anonymous Referee #2

General comments:

- *I am a new reviewer. The study is interesting and of potential great significance to relevant research on weather forecast and climate modeling. After reading through the manuscript and the authors' response to the comments from two Anonymous Referees, I find the authors do a good job in addressing most of the reviewers' comments. However, the manuscript might still need some revisions before accepted for publication in ACP. I fall between minor revision and major revision and suggest a major revision such that there will be enough time for the authors to revise.*

We thank the reviewer for the detailed and constructive comments. They are very helpful for improving the quality of the manuscript. In the revised manuscript, we added two new figures into the "supporting material" document to show the temporal variation of precipitation averaged over East China. Table 2 with the summary of statistical metrics is revised to include the RMSE metric. Other text and figures have also been revised as the reviewer suggested.

Major comments:

- *I think some of Anonymous Referee #2's comments suggest a fair evaluation. For example, "Major comments 3b: Figure 4 and 8 … whereas at V4km the precipitation magnitudes seem too positively biased over a greater area and longer time…". The authors did reply to this on timing and paid less attention to the magnitude. I understand it is very important to capture the locations of precipitation, but overestimation of precipitation is also important to note as it may cause "false alarm" in weather forecast. Please adjust some words to mention the overestimation in the model. In addition, mean bias and root mean square error are good metrics to evaluate the magnitude. The authors can provide the metrics as in Table 2.*

We agree that the magnitude is also important for predicting heavy precipitation. We did acknowledge positive biases of simulated precipitation in the manuscript as "The experiments at 16 km and 4 km with the WSM6 cloud microphysics scheme can better capture the timing and latitude of the observed precipitation event than U60km and V30km (Fig. S9 in the supporting materials), however both V16km and V4km overestimate the first peak precipitation and underestimate the second peak. The experiment at 4 km with the Thompson scheme overestimates the precipitation amount of both peaks."

We further add the discussion in the revised manuscript as "Although the simulations at convection-permitting scale with both microphysics schemes overestimate the extreme precipitation (> 10 mm/hour), the Thompson scheme produces much higher frequency of extreme precipitation than the WSM6 scheme and results in a larger positive bias relative

to the observations during this event, which deserves further investigation in future."

Now we add a new Table in the revised manuscript to include the metrics of mean bias and root mean square error. We also add more discussion about the mean biases in the revised manuscript. Some of them are listed here:

"On average of entire region as shown in Fig. 6, all the simulations overestimate the observed precipitation with the mean biases ranging from +0.59 mm/day to +5.11 mm/day (Table 2)."

"The simulation at 4 km with the Thompson scheme has much higher positive bias than the one with the WSM6 scheme (Table 2)."

"On average of entire region as shown in Fig. 10, all the simulations overestimate the observed precipitation with the mean biases ranging from +2.28 mm/day to +7.43 mm/day, except the simulation at 60 km with a small negative mean bias (Table 2). The simulation at 4 km with the WSM6 scheme has the smallest positive bias."

- *A fair evaluation also lies in other aspects:*
  (a) the spatial correlation is calculated for the selected domain and indicates the mean metric for the whole domain. However, some analysis is shifted to the rain belt. To find the locations of rain belts which the authors point out in the text, please denote the outlines of rain belt (e.g., > a selected value) or heavy rain belt (e.g., > a selected value) using contour lines.

Sorry for the confusion. Other than the spatial analysis as shown in Fig. 2, 5, 6, 10, most of other analysis focus on the average over East China (25°N-36°N, 114°E-123°E), which is denoted as the black box in Fig. 2 and 6. None of the analysis is averaged on the rain belt. Now we clarify it in all figure captions. In the captions of Fig. 2 and 6, we revise it as "The black box denotes the region of East China (25°N-36°N, 114°E-123°E) for the analysis in the following.". In the captions of Fig. 3, 4, 7, 8, 9, 11, 12, 13, we add in the text "…… averaged over East China (denoted as the black box in Fig. 2)" or "…… averaged over East China (denoted as the black box in Fig. 6)"

We did mention the rain belt in the text. Therefore, we add the contour lines of precipitation larger than 20 mm/day in the revised Fig. 2 and 6.

- *(b) From Figure 4(8) to Figure 3(7), a temporal mean is derived. Zonal mean results (magnitude) may depend on the longitude range used for the calculation. The author should explicitly mention the domain extent (I suppose the domain extends from 114 E to 122.5 E) and justify why this range is used. In addition, if zonal mean is derived, the temporal variation of precipitation can be derived and the temporal shift of precipitation in the models can be clearly shown. I suggest temporal variations can be provided (the authors can decide where to put it: in main text or supplement).*

Sorry for the confusion. Most of our analysis focus on the average over East China

(25°N-36°N, 114°E-123°E), which is denoted as the black box in Fig. 2 and 6. Now we clarify it in all figure captions. Also see our response to your comment above.

We selected this region because this study focuses on heavy precipitation of the Yangtze River Delta region (YRD) (mainly composited with three provinces: Jiangsu, Zhejiang, and Anhui, and one megacity Shanghai) as mentioned in the introduction "East China, occupied by more than 70% of the total population of China, is one of the areas with the most frequent intense extreme precipitation around the world (Zhai et al., 2005; Li et al., 2016). The socioeconomic development in regions such as the Yangtze River Delta region (YRD) in East China is remarkably vulnerable to extreme precipitation, making accurate forecast of extreme precipitation of great importance."

Now we further clarify it in the introduction as "In this study, we examine the MPAS performance in simulating a heavy precipitation event over the YRD region of East China and investigate its sensitivity to horizontal resolution and physics parameterizations."

And in the result as "Figure 3 shows the zonal averaged precipitation during the event over the YRD region of East China (25°N-36°N, 114°E-123°E, denoted as the black box in Fig. 2) from observations and simulations"

Although the temporal variation of precipitation can be derived, we think Fig. 4 and 8 can well show both latitude propagation and temporal variation. New figures of temporal variation of precipitation may not need to be put in the main text. Now we add Fig. S4 and Fig. S9 in the supporting material for the readers who are interested in.

- *(2) Section 2.1.2: Is MPAS ran in weather-forecast mode? In particular, what are the surface boundary conditions (such as SST and surface temperature/soil moisture) used for the model run? Please clarify whether it is fair to compare MPAS and GFS.*

Yes, the MPAS ran in weather-forecast mode. The surface temperature and soil moisture are simulated by the MPAS model with the Noah land surface scheme as mentioned in Section 2.1.1. The sea surface temperature is prescribed the same as the GFS forecast. Now we clarify it in the text as "The sea surface temperature (SST) is also prescribed the same as that used by the GFS forecast for the period."

- *(3) Section 2.2: I am wondering how many stations are used and what is minimum/mean/maximum distance between a station and surrounding stations. It is possible that the observations miss some extreme precipitations, which may contribute partly to the model biases relative to the current observation (e.g., overestimation mentioned earlier). In addtion, I am wondering whether data control is done on hourly data? In my opinion, evaluation of high-resolution model needs high-resolution observations. Please provide some information on the station observations.*

Over the primary region of analysis in this study, there are 511 stations. The minimum

4

distance between two stations is ~3 km, the maximum is ~70 km, and the mean is ~25 km. We clarify it in the revised manuscript as "Over the YRD region of East China (25°N-36°N, 114°E-123°E, denoted as the black box in Fig. 2), there are 511 stations. The minimum and maximum distances between two stations are ~3 km and ~70 km, respectively, and the mean is ~25 km."

We also add the discussion about the possible missing of some extreme precipitation by observations in the revised manuscript as "The coverage of observational stations with the mean distance of ~25 km between each other over the study area may not be enough and results in the missing of some extreme precipitation, which may contribute partly to the positive biases of simulations. However, since the simulations are sampled at the CMA stations, the inconsistency of comparison between observation and simulation should be reduced, particularly at the scale of 4 km."

The hourly precipitation dataset used in this study is obtained from the CMA under strict three-step quality control by station, provincial, and national departments. The methods of quality control mainly include the checking of climate threshold value, extreme value, spatial and temporal consistency and the checking through human-computer interaction. Now it is clarified in the revised manuscript "The hourly precipitation dataset from the National Meteorological Information Center of CMA is used for evaluating the simulated precipitation characteristics. In this dataset, the rainfall was measured by either tipping-buckets or self-recording siphon rain gauges, or from automatic rain gauges. The data were subject to strict three-step quality control by station, provincial, and national departments. The methods of quality control mainly include the checking of climate threshold value, extreme value, spatial and temporal consistency and the checking through human-computer interaction. All the data used in this study are quality-controlled."

Other comments:

- ***The authors should consistently set the orders of experiments in Figures 11-13 as in previous Figures 5-10: U60km.WSM6, V30km.WSM6, V16km.WSM6, V4km.WSM6, V4km.Thompson.***

Now Fig. 11-13 are revised as suggested.

- ***(2) Section 2.1.1, Lines 218-220: Since there are two options of PBL scheme, which one is used in the study?***

We add the clarification in the text as "This study used the MYNN scheme for the PBL processes."

- ***(3) Section 2.2, Lines 307-308: I cannot open https://www.ncdc.noaa.gov/data-access/model-data/model-datasets/global-forcast-system-gfs.***

We tried again on May 27 of 2019, and it is accessible. Now we add the last access date

as "" .

- *(4) Section 3.1, Lines 337-338: "with only negligible impacts from different convective parameterizations" is not clear.*

In Fig. 3, the correlation coefficients between global uniform and variable resolution simulations are 0.9 versus 0.89 (close to each other) with the GF scheme and 0.89 versus 0.86 (close to each other) with the NTD scheme. This indicates that changing convective scheme does not affect the consistency between uniform and variable resolution simulations. We revise the sentence in the text as "This comparison further indicates that the simulations at global uniform and variable resolutions are consistent with each other, and the different convective parameterizations only have negligible impact on this consistency."

- *(5) Section 3.2.3, Figure 10: It will be useful if the authors can provide a map with geographical locations of provinces, mountains, plains mentioned in the main text. The map can be put in Figure 10.*

Now the locations of the provinces and mountains mentioned in the main text are added into Fig. 10 as below:
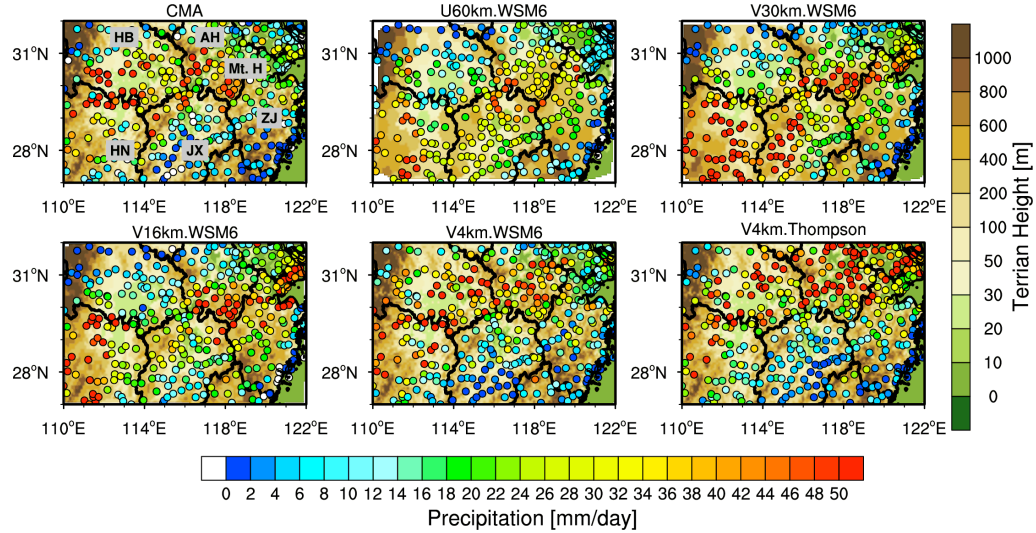

Figure 10 Spatial distributions of precipitation averaged during the event over the heavy precipitation region (27°N-32°N and 110°E-122°E) from the CMA observations and the MPAS simulations at the resolutions of 60 km, 30 km, 16 km, and 4 km. The simulations are sampled at the CMA stations. The topography is also shown. In the panel of CMA result, "AH", "ZJ", "HB", "HN", "JX", and "Mt. H" denote the provinces of Anhui, Zhejiang, Hubei, Hunan, and Jiangxi, and Mountain Huang, respectively.

- *(6) Section 3.2.3, Lines 574-575: Change "in that simulations" to "in those simulations"?*

Corrected.

- ***(7) Conclusions, Lines 609-663: The sentences can be shorten be one-third or one-half.***

This part of conclusion has been significantly shortened in the revised manuscript.

Modeling extreme precipitation over East China with a global variable-resolution modeling framework (MPASv5.2): Impacts of resolution and physics

[1]Chun Zhao, [1]Mingyue Xu, [1]Yu Wang[*], [1]Meixin Zhang, [2]Jianping Guo, [3]Zhiyuan Hu, [4]L. Ruby Leung, [5]Michael Duda, [5]William Skamarock

[1]School of Earth and Space Sciences, University of Science and Technology of China, Hefei, China

[2]State Key Laboratory of Severe Weather, Chinese Academy of Meteorological Sciences, Beijing, China

[3]Key Laboratory for Semi-Arid Climate Change of the Ministry of Education, Lanzhou University, Gansu, China

[4]Atmospheric Sciences and Global Change Division, Pacific Northwest National Laboratory, Richland, WA, USA

[5]National Center for Atmospheric Research, Boulder, CO, USA

*Corresponding authors: Yu Wang (wangyu09@ustc.edu.cn)

Key points:
1. MPAS simulations at global uniform and variable resolutions share similar characteristics of precipitation and wind in the refined region.
2. Numerical experiments reveal significant impacts of resolution on simulating the distribution and intensity of precipitation and updrafts.
3. Study provides evidence supporting the use of convection-permitting global variable-resolution simulation for studying extreme precipitation.

Abstract

     The non-hydrostatic atmospheric Model for Prediction Across Scales (MPAS-A), a global variable-resolution modeling framework, is applied at a range of resolutions from hydrostatic (60 km, 30 km, 16 km) to non-hydrostatic (4 km) scales using regional refinement over East Asia to simulate an extreme precipitation event. The event is triggered by a typical wind shear in the lower layer of the Meiyu front in East China during 25-27 June 2012 of the East Asian summer monsoon season. The simulations are evaluated using ground observations and reanalysis data. The simulated distribution and intensity of precipitation are analyzed to investigate the sensitivity to model configuration, resolution, and physics parameterizations. In general, simulations using global uniform-resolution and variable-resolution meshes share similar characteristics of precipitation and wind in the refined region with comparable horizontal resolution. Further experiments at multiple resolutions reveal the significant impacts of horizontal resolution on simulating the distribution and intensity of precipitation and updrafts. More specifically, simulations at coarser resolutions shift the zonal distribution of the rain belt and produce weaker heavy-precipitation centers that are misplaced relative to the observed locations. In comparison, simulations employing 4 km cell spacing produce more realistic features of precipitation and wind. The difference among experiments in modeling rain belt features is found mainly due to the difference of simulated wind shear formation and evolution during this event. Sensitivity experiments show that cloud microphysics have significant effects on modeling precipitation at non-hydrostatic scales, but their impacts are relatively small compared to that of convective parameterizations for simulations at hydrostatic scales. This study provides the first evidence supporting the use of convection-permitting global variable-resolution simulations for studying and improving forecasting of extreme precipitation over East China, and motivates the need for a more systematic study of heavy precipitation events and impacts of physics parameterizations and topography in the future.

2

1. Introduction

Extreme precipitation receives great attention because of its potential for generating flood, landslide, and other hazardous conditions. East China, occupied by more than 70% of the total population of China, is one of the areas with the most frequent intense extreme precipitation around the world (Zhai et al., 2005; Li et al., 2016). The socioeconomic development in regions such as the Yangtze River Delta region (YRD) in East China is remarkably vulnerable to extreme precipitation, making accurate forecast of extreme precipitation of great importance. The spatiotemporal variations of extreme precipitation over East China and their possible causes and underlying mechanisms have been investigated in many previous studies using observations and models (e.g., Ding et al., 2008; Zhang H. et al., 2011; Li et al., 2013; Zhang Q. et al., 2015, 2017; Hui et al., 2015; Liu et al., 2015; Li et al., 2016; Lin and Wang, 2016; Zhao et al., 2016; Zheng et al., 2016). Zhang et al. (2017) established a relationship between the western North Pacific subtropical high (WNPSH) and precipitation over East China and explored the underlying processes. Liu et al. (2015) analyzed data from the meteorological stations in East China and found significant increases in heavy precipitation at both rural and urban stations during 1955-2011. This enhanced precipitation intensity in East China has been partly attributed to localized daytime precipitation events (Guo et al., 2017). Recently, a regional climate model was used to simulate the regional climate extremes of China and noted large sensitivity of the simulated summer heavy precipitation over East China to the choice of cumulus parameterizations (Hui et al., 2015).

Numerical modeling is an important tool for understanding the underlying mechanisms of extreme precipitation and predicting precipitation characteristics that contributes to environmental impacts. Although precipitation modeling has improved in the last decades, accurate prediction of extreme precipitation remains challenging because of the multiscale nonlinear interactions of processes that generate heavy rainfall (Fritsch et al., 2004; Zhang et al., 2011; Sukovich et al. 2014). Although not a panacea for weather and climate modeling (NRC, 2012), previous studies suggested that increasing grid resolution could significantly improve modeling of extreme precipitation because the impacts of topography, land-use, land-atmosphere interaction, and other important processes are better resolved (e.g., Giorgi and Mearns, 1991; Giorgi and Marinucci, 1996; Leung et al., 2003; Bacmeister et al. 2014; ECMWF2016). With advances in computing and numerical modeling, convection-permitting modeling offers even more hope for reducing biases in simulating precipitation as convection and the strong vertical motions that are key to generating extreme precipitation are more

3

94 explicitly resolved (Pedersen and Winther, 2005; Déqué et al., 2007; Gao et al., 2017; Yang et
95 al. 2017; Prein et al., 2015, 2017). Previous studies suggested that convection-permitting
96 modeling is needed for more accurate prediction of the timing, distribution, and intensity of
97 extreme precipitation events over China (e.g., Zhang et al., 2013; Xu et al., 2015).

98 　　　　Most studies of convection-permitting simulations have adopted non-hydrostatic
99 regional models developed for weather forecasting or regional climate modeling (Prein et al.
100 2015). Global models capable of simulating non-hydrostatic dynamics are not as common as
101 regional models, but they offer some advantages including the ability to provide global
102 forecasts or simulations while avoiding numerical issues associated with lateral boundary
103 conditions that are major sources of uncertainty in regional modeling and also limit regional
104 feedback to large-scale circulation (e.g., Giorgi and Mearns, 1999; Wang et al. 2004; Laprise
105 et al., 2008; Leung 2013; Prein et al. 2015). Non-hydrostatic global-variable resolution models,
106 in particular, are useful as they allow convection-permitting simulations to be performed using
107 regional refinement that significantly reduces computational cost compared to global
108 convection-permitting modeling. Although global hydrostatic variable-resolution climate
109 models, such as the variable-resolution version of Community Earth System Model, have been
110 used in various applications in the last few years (e.g., Rauscher et al., 2013; Zarzycki et al.,
111 2014, 2015; Rhoades et al., 2016; Huang et al., 2016; Wu et al., 2017; Gettelman, et al., 2018;
112 Wang et al., 2018; Burakowski et al., 2019), so far few studies used global non-hydrostatic
113 variable-resolution models to investigate weather or climate simulations, particularly at
114 convection-permitting scales (e.g., Prein et al., 2015). This study explores the use of a non-
115 hydrostatic global variable resolution model, the Model for Prediction Across Scales (MPAS)
116 for modeling an extreme precipitation event in East China.

117 　　　　MPAS is a new multiscale modeling approach developed to take advantage of advances
118 in mesh generation by employing the spherical centroidal Voronoi tessellations (SCVTs) (Du
119 et al. 1999; Ringler et al. 2008). The SCVTs in MPAS enable local mesh refinement through
120 the mesh generation process where a specified scalar density function determines higher and
121 lower resolution regions in the mesh (see, e.g., Ju et al. 2011). Meshes can be configured with
122 multiple high-resolution regions, and high resolution in one region does not need to be balanced
123 by coarser resolution elsewhere. The underlying theory of SCVTs is robust concerning mesh
124 properties and mesh generation. The atmospheric solver in MPAS (Skamarock et al, 2012)
125 integrates the non-hydrostatic equations, and as such it is suitable for both weather and climate
126 simulation, i.e. for both nonhydrostatic and hydrostatic flow simulation. MPAS has been
127 evaluated and used in previous studies for investigating the resolution impact on modeling

4

128 clouds and precipitation (O'Brien et al., 2013; Zhao et al., 2016), the structure of the inter-
129 tropical convergence zone (ITCZ) (Landu et al., 2014), precipitation extremes (Yang et al.,
130 2014), atmospheric river frequency (Hagos et al., 2015), the position and strength of the eddy-
131 driven jet (Lu et al., 2015), global atmospheric predictability at convection-permitting scales
132 (Judt, 2018), and regional climate modeling (Sakaguchi et al., 2015, 2016). Except for Zhao et
133 al. (2016) and Judt (2018), the aforementioned studies used a hydrostatic version of MPAS
134 applied at resolutions ranging from ~25 km to 200 km.

135 To date, few studies have examined the MPAS performance in modeling extreme
136 precipitation events, particularly at grid scales of ~10 km or less. In this study, we examine the
137 MPAS performance in simulating a heavy precipitation event over the YRD region of East
138 China and investigate its sensitivity to horizontal resolution and physics parameterizations. A
139 heavy precipitation event that occurred on June 25-27 of 2012 over the YRD region of East
140 China is selected as it is one of the ten heaviest precipitation events in 2012. This rainfall event
141 was triggered by a typical southwest vortex in the middle and high troposphere and wind shear
142 in the lower layer of Meiyu front over East China during the East Asian summer monsoon (e.g.,
143 Xiang et al., 2013; Yao et al., 2017), initiated around 1200 UTC of 25 June. Most (more than
144 two third) of heavy precipitation events over East China were caused by wind shear associated
145 with the Meiyu front in recent decades (Yao et al., 2017). During this period, a heavy
146 precipitating system propagated along the Yangtze River and produced as much as 244 mm of
147 precipitation in 24 hours at some locations. The continuous precipitation led to 17 deaths and
148 about RMB 3.68 billion in total damage, and affected more than 685 million people in the
149 provinces of Central and East China. Simulations are performed using MPAS (v5.2) with
150 different cumulus and microphysics schemes. We first compare simulations produced using a
151 global mesh with uniform resolution and a global variable resolution mesh with a refined region
152 that has the same resolution as that of the global uniform mesh. The goal is to demonstrate the
153 fidelity of global variable resolution modeling relative to the more computationally expensive
154 global high-resolution modeling approach in regions that share the same horizontal resolution.
155 The impacts of resolutions at hydrostatic scales (with convective parameterizations) and non-
156 hydrostatic scales (i.e., convection-permitting scales with convection processes largely
157 resolved) are also examined. The MPAS simulations are evaluated against weather station
158 observations from the National Meteorological Information Center of the China
159 Meteorological Administration (CMA). In addition, the modeling results are also compared
160 with the forecasts produced by the Global Forecast System (GFS) of the National Centers for
161 Environmental Prediction (NCEP).

5

Deleted: the

Deleted: of

Deleted: last

165   The rest of the paper is organized as follows. Section 2 describes briefly the MPAS
166 model, the physics parameterizations, and the model configuration for this study, followed by
167 a description of data for evaluation. The series of global uniform and variable resolution
168 experiments are analyzed in section 3. The findings are then summarized in section 4.
169

2. Data and methodology

2.1 Model and experiments

2.1.1 MPAS-Atmosphere (MPAS-A) model

173   This study uses a fully compressible non-hydrostatic model (MPAS v5.2) developed
174 for weather prediction and climate applications. The non-hydrostatic dynamical core of MPAS
175 is described in Skamarock et al. (2012). MPAS uses C-grid staggering of the prognostic
176 variables and centroidal Voronoi meshes to discretize the sphere. The unstructured spherical
177 centroidal Voronoi tessellation (SCVT) generation algorithms can provide global quasi-
178 uniform resolution meshes as well as variable-resolution meshes through the use of a single
179 scalar density function, hence opening opportunities for regional downscaling and upscaling
180 between mesoscales and non-hydrostatic scales to hydrostatic scales within a global framework.
181 The vertical discretization uses the height-based hybrid terrain-following coordinate (Klemp,
182 2011), in which coordinate surfaces are progressively smoothed with height to remove the
183 impact of small-scale terrain structures. The dynamical solver applies the split-explicit
184 technique (Klemp et al., 2007) to integrate the flux-form compressible equations. The basic
185 temporal discretization uses the third order Runge-Kutta scheme and explicit time-splitting
186 technique (Wicker and Skamarock, 2002), similar to that used in the Weather Research and
187 Forecasting (WRF) model (Skamarock et al., 2008). The scalar transport scheme used by
188 MPAS on its Voronoi mesh is described in Skamarock and Gassmann (2011), and the
189 monotonic option is used for all moist species. The extensive tests of MPAS using idealized
190 and realistic cases verify that smooth transitions between the fine- and coarse-resolution
191 regions of the mesh lead to no significant distortions of the atmospheric flow (e.g., Skamarock
192 et al., 2012; Park et al., 2013).
193   In the current version (v5.2) of MPAS, there are a few physics schemes available. Three
194 convective parameterizations can be used. The Kain-Fritsch (KF, Kain, 2004) and the new
195 Tiedtke (NTD, Bechtold et al., 2004, 2008, 2014) schemes represent both deep and shallow
196 convection using a mass flux approach with a convective available potential energy (CAPE)
197 removal time scale (Kain, 2004). The third one, the GF scheme (Grell and Freitas, 2014), is

6

198 based on the Grell-Devenyi ensemble scheme (Grell and Devenyi, 2002) using the multi-
199 closure, multi-parameter, ensemble method but with improvements to smooth the transition to
200 cloud-resolving scales following Arakawa et al. (2011). This scale-awareness is critical for
201 global variable resolution simulation across hydrostatic (e.g., tens of km) and non-hydrostatic
202 scales (e.g., 4 km). Fowler et al. (2016) implemented the GF convective parameterization in
203 MPAS and examined the impacts of horizontal resolution on the partitioning between
204 convective-parameterized and grid-resolved precipitation using a variable-resolution mesh in
205 which the horizontal resolution varies between hydrostatic scales (~50 km) in the coarsest
206 region of the mesh to non-hydrostatic scales (~ 3 km) in the most refined region of the mesh.
207 For cloud microphysics, the WSM6 (Hong and Lim, 2006) and Thompson (Thompson et al.,
208 2008) schemes, both of which are bulk microphysical parameterizations, are selected and
209 compared. Both schemes include six hydrometeor species: water vapor, cloud water, rain,
210 cloud ice, snow, and graupel (Gettelman et al., 2019). The WSM6 scheme is a one-moment
211 prognostic parameterization, while the Thompson scheme includes a two-moment prognostic
212 parameterization for cloud ice and the single-moment parameterization for the other
213 hydrometeor species. The two schemes apply the same formula of gamma distribution of
214 hydrometeor species: $N(D) = N_0 D^\mu e^{-\lambda D}$, where D is the particle diameter, N_0 is the intercept
215 parameter, μ is the shape factor, and λ is the slope parameter, although the parameter values or
216 functions vary in the two schemes. The mass-size relationship in WSM6 and Thompson is also
217 expressed in the same formula as $m(D) = aD^b$. The mean falling speed is calculated as
218 $V(D) = cD^d(\frac{\rho_0}{\rho})^{0.5}$ in WSM6 and $V(D) = cD^d(\frac{\rho_0}{\rho})^{0.5}exp(-fD)$ in Thompson, respectively
219 (Hong and Lim, 2006; Thompson et al., 2008). In the formula, the WSM6 scheme assumes a
220 power-law fit between terminal velocity and particle size as Locatelli and Hobbs (1974), while
221 the Thompson scheme incorporates an exponential decay parameter to allow for a decrease in
222 falling speed with increasing size (Molthan et al., 2012). Two options are available for
223 representing the planetary boundary layer (PBL) processes, the Mellor-Yamada-Nakanishi-
224 Niino (MYNN) scheme (Nakanishi and Niino, 2006 and 2009) and the YSU scheme (Hong et
225 al., 2006; Hong 2010). This study used the MYNN scheme for the PBL processes. The Noah
226 scheme (Chen and Dudhia, 2001) and the RRTMG scheme (Mlawer et al., 1997; Iacono et al.,
227 2000) were implemented, respectively, for the land surface and radiative transfer processes.
228
229 *2.1.2 Numerical experiments*

7

230   In this study, the height coordinate of MPAS is configured with 55 layers, and the model
231 top is at 30 km. Multiple experiments are conducted with MPAS using quasi-uniform
232 resolution meshes and variable resolution meshes. Two quasi-uniform resolution meshes and
233 three variable resolution meshes are configured, similar to those shown in Figure 1a and b that
234 are coarsened to display the structure of the individual mesh cells. The quasi-uniform mesh has
235 essentially the same mesh spacing globally, while the variable resolution mesh has finer mesh
236 spacing in the refined region with a transition zone between the fine and coarse resolution
237 meshes. More details about the mesh generation can be found in Ringler et al. (2011). The two
238 quasi-uniform meshes have grid spacing that approximately equals to 15 km (U15km) and 60
239 km (U60km). The three variable resolution meshes feature a circular refined high-resolution
240 region centered over East China as shown in Figure 1c. Figure 1c shows the exact mesh size
241 distribution of the 4-60km variable resolution mesh (V4km) that has a refined region with grid
242 spacing of approximately 4 km, and the mesh spacing gradually increases through a transition
243 zone to approximately 60 km for the rest of the globe. The other two variable resolution meshes
244 (V16km and V30km) have a similar mesh structure as the V4km mesh but with a mesh spacing
245 of 16 km and 30 km, respectively, over the refined region that gradually increases to 128 km
246 and 120 km, respectively, elsewhere.
247   Experiments U15km and V16km are compared to examine the difference between
248 global uniform and variable resolution simulations in capturing the precipitation in the refined
249 region, in order to explore the potential of regional refinement for regional weather and climate
250 simulation. It is noteworthy here that the U15km mesh comprises ~2.5 million cells and the
251 V16km mesh only comprises ~0.11 million cells. The difference in the number of mesh cells
252 leads to a difference in computational and storage demand. With the TH-2 supercomputer of
253 National Supercomputer Center in Guangzhou (NSCC-GZ), it takes ~9000 CPU hours and
254 ~240 CPU hours to finish a one-day simulation for U15km and V16km, respectively. In
255 addition, with the standard MPASv5.2, the sizes of output data per one-day simulation for
256 U15km and V16km are 0.5 T and 0.02 T, respectively. The same time step of 60 second is used
257 for physics and dynamics for both U15km and V16km simulations. In order to investigate the
258 potential impact from physics parameterizations, two available convective parameterizations
259 (GF and NTD) are used for each experiment with the two meshes. Two cloud microphysics
260 schemes (WSM6 and Thompson) are also tested, but the precipitation differences in the U15km
261 and V16km experiments are small. Therefore, only the results using WSM6 with two different
262 convective parameterizations are shown in this study for the two meshes (U15km.NTD,
263 U15km.GF, V16km.NTD, and V16km.GF).

8

264　The U60km, V30km, V16km, and V4km experiments are conducted to quantify the impacts
265　of horizontal resolution on simulating precipitation characteristics. The numbers of grid cells
266　in the U60km, V30km, V16km, and V4km meshes are ~0.16 million, 0.10 million, ~0.11
267　million, and ~0.8 million, respectively. Difference in the number of cell and minimum cell size
268　also leads to a difference in computational and storage demand. With the TH-2 supercomputer
269　of NSCC-GZ, it takes ~200 CPU hours, ~150 CPU hours, ~240 CPU hours, and ~1800 CPU
270　hours to finish a one-day simulation for U60km, V30km, V16km, and V4km meshes,
271　respectively. In addition, with the standard MPASv5.2, the sizes of output data per one-day
272　simulation for the four meshes are 0.03 T, 0.02 T, 0.02 T, and 0.15 T, respectively. The time
273　steps used for physics and dynamics for the four meshes are 300 seconds, 120 seconds, 60
274　seconds, and 20 seconds, respectively.

275　　　As discussed above, GF is the only convective parameterization that has been tested
276　with scale-aware capability for using across the hydrostatic (e.g., tens of km) and non-
277　hydrostatic scales (e.g., 4 km). Therefore, in order to investigate the difference among the
278　experiments with the four meshes (U60km, V30km, V16km, and V4km), they are all
279　conducted with the GF convective parameterization. Since the cloud microphysics has
280　significant impact on the V4km simulations (discussed latter), the experiments of V4km with
281　both WSM6 (V4km.WSM6) and Thompson (V4km.Thompson) cloud microphysics schemes
282　are analyzed in this study. When examining the difference between the global uniform and
283　variable resolution simulations and investigating the impact of mesh spacing, the same physics
284　schemes and parameter values are used in multiple experiments if not specified explicitly. All
285　the numerical experiments discussed above are summarized in Table 1.

286　　　Due to the large computing cost and data storage of the experiments conducted,
287　particularly for the U15km and V4km experiments, this study does not perform ensemble
288　simulations. Instead, the bootstrapping statistical analysis is used to test the statistical
289　significance of the difference among multiple experiments investigated in this study. The
290　bootstrap method uses resampling technique to extract certain samples, called bootstrap
291　samples, within the range of the original data. Statistical metrics, such as averages, variances,
292　correlation coefficient, can be calculated for each bootstrap sample. For a given confidence
293　level (e.g., 95%), bootstrap confidence intervals of specific statistical metric can be estimated
294　(e.g., Efron, 1992; Efron and Tibshirani, 1994).

295　　　To simulate the heavy precipitation event that occurred during June 25-27 of 2012 over
296　the YRD of East China, all the MPAS experiments were initialized at 0000 UTC of 23 June
297　2012 to allow appropriate spin-up time, and the modeling results for 25-27 June 2012 are

9

298 analyzed. The simulations were initialized using the analysis data at 1° horizontal resolution at
299 0000 UTC of 23 June 2012 from the Global Forecast System (GFS) of National Center for
300 Environmental Prediction (NCEP), the same as that used by the GFS forecast for the period.
301 The sea surface temperature (SST) is also prescribed the same as that used by the GFS forecast
302 for the period. This way, the MPAS simulation results can also be compared against the GFS
303 forecast starting from the 0000 UTC of 23 June 2012.

304 **2.2 Dataset**

305   Several datasets are used to evaluate the MPAS simulations. The hourly precipitation
306 dataset from the National Meteorological Information Center of CMA is used for evaluating
307 the simulated precipitation characteristics. In this dataset, the rainfall was measured by either
308 tipping-buckets or self-recording siphon rain gauges, or from automatic rain gauges. The data
309 were subject to strict three-step quality control by station, provincial, and national departments.
310 The methods of quality control mainly include the checking of climate threshold value, extreme
311 value, spatial and temporal consistency and the checking through human-computer interaction.
312 All the data used in this study are quality-controlled. The distribution of stations over the study
313 domain is shown as the color-filled circles in Figure 2. Over the YRD region of East China
314 (25°N-36°N, 114°E-123°E, denoted as the black box in Fig. 2), there are 511 stations. The
315 minimum and maximum distances between two stations are ~3 km and ~70 km, respectively,
316 and the mean is ~25 km. The hourly wind field dataset from the ECMWF Reanalysis (ERA5)
317 (0.28°×0.28°) (https://rda.ucar.edu/datasets/ds630.0/) is used as the reference for evaluating the
318 simulated distributions of winds. Lastly, the global forecast products at 0.5° and 1° horizontal
319 resolutions starting from UTC00 of 23 June 2012 are also used for comparison. The GFS
320 forecast products are downloaded from https://www.ncdc.noaa.gov/data-access/model-
321 data/model-datasets/global-forcast-system-gfs (last access on May 27 of 2019). Since the focus
322 of this study is not to investigate the difference between MPAS and GFS or to evaluate the
323 performance of GFS, details about the GFS are not discussed here but can be found on the
324 website listed above.
325

326 **3. Results**

327 **3.1 Simulations at quasi-uniform and variable resolutions**

328   Figure 2 shows the spatial distributions of precipitation and wind at 850 hPa averaged
329 during the event (June 25 00:00 to June 27 12:00 UTC Time) from the simulations with global
330 uniform (15 km) and variable (16 km over East China) resolutions (U15km.NTD and

Deleted:

Deleted: .

10

333 V16km.NTD). The mean precipitation from the CMA stations and the winds from the ERA-
334 interim reanalysis are also shown. The CMA observations show average precipitation rate
335 exceeding 50 mm/day over central East China with a heavy rain belt extending from west to
336 east along 31°N. The rain belt is associated with the wind shear near the surface that is typically
337 accompanied with the Meiyu front during the East Asian summer monsoon. In general, both
338 simulations capture the observed precipitation pattern. It is evident that the modeling results
339 over the refined region are consistent between the uniform and variable resolution simulations.
340 The spatial correlation coefficient between the two simulations over the refined region (entire
341 region shown in Fig. 2) is 0.85. Besides precipitation, both simulations also capture the
342 distribution of winds from the reanalysis data. The wind fields between the two simulations are
343 also consistent with a spatial correlation coefficient of 0.99.

344   As mentioned above, the precipitation during this event is concentrated in a west-east
345 narrow belt. For a more quantitative comparison, Figure 3 shows the zonal averaged
346 precipitation during the event over the YRD region of East China (25°N-36°N, 114°E-123°E,
347 denoted as the black box in Fig. 2) from observations and simulations. The CMA observations
348 show an evident precipitation peak reaching ~40 mm/day around the latitude of 31°N. All four
349 simulations with different resolutions and convective parameterizations capture well the zonal
350 distribution of observed precipitation. The correlation coefficients are 0.9 and 0.89 for the
351 U15km and V16km simulations with the GF scheme, respectively, and 0.89 and 0.86 for the
352 same simulations but with the NTD scheme. This comparison further indicates that the
353 simulations at global uniform and variable resolutions are consistent with each other, and the
354 different convective parameterizations only have negligible impact on this consistency.
355 Although this consistency does not depend on the convective schemes, simulations with the
356 GF parameterization produce larger peak precipitation than those with the NTD
357 parameterization and are more consistent with observations for this event. The impact of cloud
358 microphysics (WSM6 and Thompson) on the consistency in modeling total precipitation is also
359 examined and is found to be negligible (Fig. S1 and S2 in the supporting materials), although
360 there are some impacts on the simulated grid-resolved precipitation (Fig. S3 in the supporting
361 material).

362   Figure 4 shows the meridional precipitation propagation over East China (denoted as
363 the black box in Fig. 2) during the event. The CMA observations indicate that the rain belt
364 propagates from 26°N at 06 UTC of 25 June to 31°N at 00 UTC of 26 June and includes two
365 precipitation peaks around 31°N. The rainfall reaches the first peak around 00 UTC of 26 June.

11

Formatted: Font color: Auto
Formatted: Font color: Auto
Formatted: Font color: Auto
Formatted: Font color: Auto
Formatted: Font color: Auto
Formatted: Font color: Auto
Formatted: Font color: Auto
Formatted: Font color: Auto
Formatted: Font color: Auto

Deleted: with only
Deleted: s from different convective parameterizations.

368   The rain belt stays around 31°N and reaches the second peak around 00 UTC of 27 June. The

369   event ends around 12 UTC of 27 June (Fig. S4 in the supporting material). The first

370   precipitation peak was generated by the southwest-northeast wind shear line formed over

371   Central East China along with a vortex over the Southwest at 00 UTC of 26 June. The shear

372   line gradually extended eastward, leading to the second precipitation peak around 00 UTC of

373   27 June (Fig. S5 in the supporting material). All four experiments generally simulate the

374   southwest vortex and wind shear during the event, although the strength and location do not

375   match perfectly with the reanalysis. As the large-scale environment is quite well represented

376   in the model, the simulations also generally capture the two peaks of precipitation along 31°N

377   as observed. However, both U15km and V16km simulate a broader rain belt, resulting in

378   positive biases of precipitation south of 30°N (Fig. S6 in the supporting materials). Both

379   simulations shift the first peak precipitation southward. In addition, the simulations extend the

380   first peak precipitation period and shorten the second one to some extent (Fig. S6 in the

381   supporting materials). The lower averaged total precipitation around 31°N from the simulation

382   with the NTD parameterization (Fig. 3) is mainly due to the lower rainfall before 26 June

383   compared to the one with the GF parameterization (Fig. S6). For the two precipitation peaks,

384   the simulation with NTD is comparable to the one with GF. Although the two convective

385   parameterizations lead to significant difference in simulating total precipitation before 26 June,

386   both simulations generate consistent wind circulations at 700 hPa before 26 June with spatial

387   correlation coefficients above 0.9 (over the domain as shown in Fig. S5 in the supporting

388   material). Although the two convective parameterizations lead to different total precipitation,

389   they have negligible impact on the consistency in modeling precipitation propagation using

390   uniform and variable resolutions during this event. The correlation coefficients are 0.48 and

391   0.42 for the simulations with the GF scheme at the resolutions of U15km and V16km,

392   respectively, and 0.55 and 0.54 for the simulations with the NTD scheme at the two resolutions.

393   The results again indicate the consistency between the simulations at the global uniform and

394   variable resolutions at hydrostatic scale over the refined region regardless of the convective

395   parameterization used.

396   Overall, for the selected event, the MPAS simulations at global uniform and variable

397   resolutions produce consistent results over the refined region with comparable horizontal

398   resolution in terms of the spatial patterns of precipitation and wind fields and the precipitation

399   propagation. This finding is in general agreement with the findings by previous studies of

400   MPAS with idealized experiments (e.g., Zhao et al., 2016) and real-world experiments (e.g.,

12

Deleted: S4

Deleted: S5

Deleted: S5

Deleted: S5

Deleted: S4

406   Sakaguchi et al., 2015). These findings provide the basis for using global variable resolution

407   configurations of MPAS for modeling extreme precipitation over East China. In the following,

408   the impacts of resolution on modeling extreme precipitation during this event are investigated

409   with multiple global variable-resolution experiments.

410

411   **3.2 Impacts of resolution**

412   *3.2.1 Parameterized and resolved precipitation*

413   Multiple experiments using MPAS at various resolutions are conducted as stated in the

414   methodology section. The resolution crosses the scales from 60 km, 30 km, 16 km to 4 km. For

415   global variable resolution configurations, a scale-aware convective parameterization is needed,

416   especially for the configuration that crosses the hydrostatic (convective parameterization is

417   required) and non-hydrostatic scales (convection-permitting). Therefore, the experiments

418   analyzed below are all conducted with the GF scheme that is developed for simulations down

419   to ~ 4 km resolution (details can be found in Grell and Freitas, 2014). To demonstrate the scale-

420   aware performance of the GF convective parameterization across various resolutions, Figure 5

421   shows the spatial distributions of convective parameterized and resolved precipitation averaged

422   during the event. At the resolution of 60 km and 16 km, precipitation produced from the

423   convective parameterization dominates the total precipitation amount. On the contrary, at the

424   resolution of 4 km, the total precipitation amount from simulations with two different

425   microphysics is dominated by the resolved precipitation. The fraction of parameterized

426   precipitation in the total decreases significantly from the simulations at 16 km to the ones at

427   4km over the heavy precipitation region (Fig. S7 in the supporting materials). It is also

428   interesting that the fraction of parameterized precipitation increases from the simulations at 60

429   km to the ones at 16 km to some extent. This demonstrates that the GF scheme is aware of the

430   resolution change so the precipitation from the simulations at convection-permitting scale is

431   mostly produced by the cloud microphysics in MPAS.

432   *3.2.2 Spatial and temporal variation*

433   Figure 6 shows the observed and simulated spatial distributions of precipitation and

434   wind fields at 850 hPa averaged during the event. For comparison, the GFS forecast results at

435   the resolutions of 1.0 degree and 0.5 degree are also included. The GFS forecast results from

436   the two resolutions are similar, both showing a northward shifted rain belt compared to the

437   CMA observation. Due to the northern shift of the rain belt, the spatial correlation coefficients

438   between the GFS and the CMA observations over the entire region of Fig. 6 are only 0.06 and

Deleted: S6

13

440 0.03 for the resolutions of 1.0 degree and 0.5 degree, respectively. In comparison, the spatial
441 correlation coefficients between the CMA observations and the MPAS simulations at the
442 resolutions of 60 km, 30 km, and 16 km are 0.49, 0.47, and 0.56, respectively. The correlation
443 coefficients for the 4 km simulations with the WSM6 and Thompson microphysics schemes
444 are 0.63 and 0.54, respectively. In general, the experiments at the convection-permitting scale
445 (4 km) capture better the observed precipitation pattern than simulations with convective
446 parameterization over the refined region, although the performance is affected by the
447 microphysics scheme to some extent. On average of the entire region as shown in Fig. 6, all
448 the simulations overestimate the observed precipitation with the mean biases ranging from
449 +0.59 mm/day to +5.11 mm/day (Table 2).

450 In order to test the statistical significance of the difference in spatial distributions
451 among the experiments, the 95% confidence intervals of spatial correlation are estimated based
452 on the bootstrap analysis. Although the correlation coefficients estimated above have an
453 uncertain range, at the 95% confidence level the results still indicate that the V16km simulation
454 produces better spatial pattern of precipitation than other hydrostatic-scale simulations. In
455 addition, the simulation at the convection-permitting scale is comparable to, if not better than,
456 the V16km simulation. The results are summarized in Table 3. It is noteworthy that, although

457 the difference in precipitation over East China is significant among the GFS forecasts at 0.5°
458 and 1.0° resolutions and MPAS at various resolutions, their global distributions of precipitation
459 and wind averaged during the event period are similar with spatial correlation coefficients of
460 0.40-0.43 (precipitation) and 0.86-0.93 (wind), respectively, against the satellite retrieved
461 precipitation and ERA5 reanalysis wind (Fig. S8 in the supporting material).

462 The zonal distributions of precipitation can better demonstrate the difference among
463 the simulations. Figure 7 shows the observed and simulated zonal distributions of precipitation
464 averaged during the event over the YRD region of East China. For comparison, the GFS
465 forecasts at 1°and 0.5° resolutions are also included. The modeling results are sampled at the
466 CMA stations. Consistent with the spatial distributions of precipitation shown in Fig. 6, the
467 GFS forecasts at both 0.5° and 1.0° resolutions reproduce the precipitation peak of ~40 mm/day
468 but shift the rain belt northward by about 4.0° latitude from 31°N to 35°N. The MPAS
469 simulations at 16 km and 30 km with the GF scheme can well capture the peak precipitation
470 around 31°N, although the simulation at 30 km produces a second lower peak of precipitation
471 around 29°N. The simulation at 60 km produces much lower precipitation peak of ~25 mm/day
472 and shifts the rain belt southward to around 30°N. The underestimate of the simulation at 60

14

475　km is mainly due to the underestimate of the convective parameterized rain (Fig. 5). It is
476　noteworthy that on regional average the simulation at 60 km overestimates the observed
477　precipitation with the mean bias of +2.18 mm/day (Table 2). For the two MPAS simulations at
478　4 km, the precipitation is mainly generated by cloud microphysics (Fig. 5) and therefore can
479　be significantly affected by the cloud microphysics schemes. The MPAS simulations at 4 km
480　with WSM6 and Thompson produce different zonal distributions of the rain belt. The
481　simulation using WSM6 reproduces the peak of precipitation, while the simulation using
482　Thompson produces higher precipitation with a peak at 50 mm/day and shifts the peak
483　northward by about 1 degree. The simulation at 4 km with the Thompson scheme has much
484　higher positive bias than the one with the WSM6 scheme (Table 2). Overall, the correlation

<div style="float:right; border:1px solid #000; padding:2px;">**Deleted:**</div>

485　coefficients between the CMA observations and the GFS forecasts are -0.19 and -0.15 for 0.5°
486　and 1.0°, respectively, and the correlation coefficients are 0.68, 0.71, 0.89, and 0.97 (0.72) for
487　the MPAS simulations at 60 km, 30 km, 16 km, and 4 km with the WSM6 (Thompson) cloud
488　microphysics. At the 95% confidence level, the difference among the experiments is significant
489　(Table 3).

<div style="float:right; border:1px solid #000; padding:2px;">**Deleted:** 2</div>

490　　　　Figure 8 compares the observed and simulated precipitation propagation during the
491　event over East China. The modeling results are sampled at the CMA stations. The GFS
492　forecasts at 0.5° and 1.0° are similar, and both generate a heavy precipitation zone between
493　34°N and 35°N that lasts for about 18 hours from UTC12 of June 26. This is largely different
494　from the CMA observations, so the correlation coefficients between the forecasts and
495　observations are only 0.02 and 0.03 for 0.5° and 1.0°, respectively. The northward shift of rain
496　belt during the event (shown in Fig. 6 and 7) is related to the GFS forecast that only produced
497　the second peak of precipitation around UTC 0000 of 27 June while totally missing the first
498　peak (Fig. S9). In addition, the GFS forecast overestimates the second peak and shift it towards
499　the north by about 4°. The timing and location shift of the rain belt in the GFS forecast are
500　mainly because of the bias of GFS in simulating the wind shear in this event. The GFS forecast
501　failed to produce the southwest-northeast wind shear line around UTC 0000 of 26 June and
502　generated too broad vortex over the west. Around UTC 0000 of 27 June, GFS simulated the
503　wind shear line but locating it further north (Fig. S10 in the supporting material).

<div style="float:right; border:1px solid #000; padding:2px;">**Deleted:** S8</div>

504　　　　The MPAS simulations are highly dependent on the resolutions. All simulations
505　roughly produce the two peaks of precipitation as observed during the event. However, the
506　experiment at 60 km simulates the first precipitation peak southward and the second peak
507　northward of the observations, while the experiment at 30 km simulates the second peak further

15

south and a few hours earlier. The time and location shift corresponding well to biases in simulated wind shear (Fig. S10). The spatial correlation coefficients of precipitation are 0.30 and 0.32 between the observations and the simulations at 60 km and 30 km, respectively. The experiments at 16 km and 4 km with the WSM6 cloud microphysics scheme can better capture the timing and latitude of the observed precipitation event than U60km and V30km (Fig. S11 in the supporting materials), however both V16km and V4km overestimate the first peak precipitation and underestimate the second peak. The experiment at 4 km with the Thompson scheme overestimates the precipitation amount of both peaks. Overall, all the simulations overestimate the observed precipitation during the event (Table 2). The correlation coefficients are 0.41 and 0.42 (0.38) for 16 km and 4 km with the WSM6 (Thompson) cloud microphysics schemes, respectively. At the 95% confidence level (Table 3), the experiments at 16 km and 4 km are comparable in terms of simulating the propagation of this rain belt and better than the experiments at other resolutions. It is interesting to note that MPAS and GFS forecasts, sharing the same initial condition, simulate different large-scale circulation particularly the wind shear structure with the system evolving (Fig. S10). The model capability in successfully capturing the wind shear structure during this event determines the performance in generating the rain belt evolution. The formation and evolution of wind shear during the Meiyu front over East China have been found interacting with multiscale processes and systems, including terrain and convective latent heat (Yao et al., 2017). Different representation of the terrain over East China in various resolutions may impact the simulated wind shear structure. Previous studies also found that convective latent heat may vary with resolutions and physics (Hagos et al., 2013; Zhao et al., 2016), which can further affect the simulation of wind shear structure. Therefore, the difference in resolution and physics between MPAS and GFS may result in their difference in simulating the formation and evolution of wind shear structure during the event. A more detailed exploration of the differences between the MPAS and GFS simulations is beyond the scope of this study.

The spatial distribution of the rain belt can also be reflected by the vertical wind distributions. Figure 9 compares the height-latitude cross section of the winds averaged over the region (shown as in Fig. 6) during the event from the ERA5 reanalysis, the GFS forecasts, and the MPAS simulations. In the ERA5 reanalysis wind fields, vertical motion is located primarily around 31°N, extending from the lower troposphere (~900 hPa) to the upper troposphere (~200 hPa). The GFS simulates the vertical motion primarily around 33°N, but the vertical motion is also strong around 35°N from 600 hPa to 200 hPa, which can be linked to

16

Deleted: S8

Deleted: S9

Deleted: 2

Deleted: S8

548 the heavy precipitation generated there. These biases result in weaker correlation in vertical
549 winds between the reanalysis and the GFS forecasts with coefficients of 0.29 and 0.32 for 0.5°
550 and 1.0° resolutions, respectively. The MPAS experiment at 60 km simulates the vertical
551 motion toward the south around 28°N. The MPAS experiments at 30 km and 16 km generally
552 agree well with the ERA5 reanalysis, although both generate higher vertical motion in the south
553 (e.g. 25°N) to some extent. The correlation coefficients between the reanalysis and the MPAS
554 experiments at 60 km, 30 km, and 16 km are 0.53, 0.68, and 0.80, respectively. The MPAS
555 experiment at 4 km with the WSM6 scheme produces consistent vertical motion with that in
556 the ERA5 reanalysis, while the one with the Thompson scheme shifts the vertical motion a
557 little further north. Both experiments at 4 km have the highest correlation in the distributions
558 of vertical motion with the reanalysis with coefficients of 0.85 and 0.80 for WSM6 and
559 Thompson, respectively. The statistical significance tests based on the bootstrap analysis
560 indicate that at the 95% confidence level the model performance at 16 km and 4 km in terms
561 of simulating vertical structure of winds are comparable and better than the simulations at
562 coarser resolution (Table 3). The zonal distributions of precipitation discussed above
563 correspond well with the distributions of vertical motion in all the experiments. Differences in
564 the spatial distribution of vertical motions suggest that model resolution, and in some degree
565 cloud microphysics parameterizations, have important effects on simulating the structure of the
566 wind shear over East China during the East Asian summer monsoon and the embedded
567 precipitation.
568
569 *3.2.3 Distribution of extreme precipitation*
570   Besides predicting the spatial and temporal variations of the rain belt, it is also critical
571 to capture the location and intensity of extreme precipitation within the heavy rain belt. Since
572 the GFS forecasts shift the entire rain belt northward, only the MPAS simulations are analyzed
573 here. Figure 10 shows the spatial distributions of precipitation averaged during the event over
574 the heavy rain region (27°N-32°N and 110°E-122°E). The CMA observations show that heavy
575 precipitation exceeding 50 mm/day mainly occurs over the plains of South Anhui province and
576 Southeast Hubei province and part of the Huang Mountains. The MPAS experiment at 60 km
577 simulates much smaller areas with heavy precipitation exceeding 50 mm/day. In addition, it
578 simulates heavy precipitation over some areas of Hunan province, which is not observed by
579 the CMA stations. The experiment at 30 km produces more numerous areas with heavy
580 precipitation and captures the locations of heavy precipitation over the Huang Mountains.

Deleted: 2

17

582 However, it misses the heavy precipitation over the plains of South Anhui province and
583 Southeast Hubei province; instead, it produces heavy precipitation over large areas of
584 mountainous regions over Hunan and Jiangxi provinces. The experiment at 16 km simulates
585 better spatial distribution of heavy precipitation, particularly capturing the heavy precipitation
586 over the Huang Mountains and the plain of South Anhui province, although it still shifts the
587 heavy precipitation from Southeast Hubei province to Hunan province. The experiments at 4
588 km are affected by the cloud microphysics. The 4 km experiment with the WSM6 scheme
589 produces the best spatial distribution among the MPAS experiments. It generally captures the
590 observed heavy precipitation areas during this event as discussed above, although the locations
591 do not perfectly match that of the observations. On the other hand, the 4 km experiment with
592 the Thompson microphysics produces more areas of heavy precipitation over Central Anhui
593 province. As a result, the correlation coefficients between the observations and the MPAS
594 experiments at the resolutions of 60 km, 30 km, 16 km, and 4 km are 0.20, 0.21, 0.29, 0.50
595 (WSM6), and 0.42 (Thompson), respectively. The statistical significance test based on the
596 bootstrap analysis indicates that at the 95% confidence level the simulations at 4 km can better
597 capture the spatial distribution of heavy precipitation than the simulations at resolutions of
598 hydrostatic scale (Table 3). On average of the entire region as shown in Fig. 10, all the
599 simulations overestimate the observed precipitation with the mean biases ranging from +2.28
600 mm/day to +7.43 mm/day, except the simulation at 60 km with a small negative mean bias
601 (Table 2). The simulation at 4 km with the WSM6 scheme has the smallest positive bias.
602   Figure 11 shows the probability density functions (PDFs) of hourly precipitation at all
603 the CMA stations over East China during the event. The simulations are sampled at the CMA
604 stations. Precipitation above ~5 mm/hour (~120 mm/day) is considered very heavy and extra
605 heavy storm rain event (refer to the CMA definition) that may cause dramatic flooding and
606 damage locally or regionally. During this event, for precipitation lower than ~5 mm/hour, the
607 MPAS simulations at hydrostatic scales (60 km, 30 km, and 16 km) overestimate the frequency,
608 while above ~5 mm/hour, these simulations significantly underestimate the frequency. In
609 contrast, the MPAS simulations at convection-permitting scale (4 km) produce much higher
610 frequency of extreme precipitation above ~5 mm/hour, more consistent with the observations.
611 However, the simulated frequency of extreme precipitation at convection-permitting scale
612 depends on the cloud microphysics schemes. Although the simulations at convection-
613 permitting scale with both microphysics schemes overestimate the extreme precipitation (> 10
614 mm/hour), the Thompson scheme produces much higher frequency of extreme precipitation
615 than the WSM6 scheme and results in a larger positive bias relative to the observations during

18

618 this event, which deserves further investigation in future. The coverage of observational
619 stations with the mean distance of ~25 km between each other over the study area may not be
620 enough and results in the missing of some extreme precipitation, which may contribute partly
621 to the positive biases of simulations. However, since the simulations are sampled at the CMA
622 stations, the inconsistency of comparison between observation and simulation should be
623 reduced, particularly at the scale of 4 km. The results also indicate that the convective
624 parameterization appears not to be able to produce the higher intensity precipitation.

625 Previous studies found that the distribution of extreme precipitation correlates well with
626 that of the lower tropospheric upward vertical velocity (e.g., Zhao et al., 2016). Figure 12 shows
627 the PDFs of hourly upward vertical velocity averaged below 700 hPa at all the CMA stations
628 during the event from the MPAS simulations. In general, the comparison of lower-level upward
629 vertical velocity among the experiments is consistent with that of precipitation (Fig. 11) in
630 those simulations at hydrostatic scales (i.e., 60 km, 30 km, and 16 km in this study) produce
631 higher frequencies of updrafts < 4 cm/s than simulations at 4 km and vice versa for stronger
632 updrafts. The difference in updrafts between the 4 km MPAS simulations with two different
633 cloud microphysics schemes is negligible. Another analysis with the simulated updrafts at
634 various resolutions all regridded to 0.5° resolution shows the similar PDFs as Fig. 12. Previous
635 studies have proposed some mechanisms underlying the resolution impacts on modeling
636 vertical velocity (e.g., Rauscher et al., 2016; Jeevanjee et al., 2017; Herrington and Reed, 2017;
637 O'Brien et al., 2016; Fildier et al., 2018). Among these mechanisms, Rauscher et al. (2016)
638 argued that the resolution-dependent vertical velocity is caused by the interaction between the
639 constraint of fluid continuity and macro-scale turbulence. They suggested that the vertical
640 velocity should be more intense at higher resolution because the horizontal velocity increment
641 follows approximately a power law of resolution. Therefore, the resolved vertical transport
642 must increase as grid spacing decreases. Assuming atmospheric moisture is relatively
643 insensitive to resolution, the upward moisture flux should increase as grid spacing decreases,
644 hence producing more precipitation.

645 Figure 13 shows the PDFs of the upward moisture flux and the relationship between
646 hourly precipitation versus upward moisture flux at 850hPa during the event from the MPAS
647 simulations at 60km, 30km, 16km and 4km. It is evident that the simulations at higher
648 resolutions produce more frequent intense upward moisture fluxes at 850hPa, consistent with
649 Rauscher et al. (2016) and O'Brien et al. (2016). Rauscher et al. (2016) found a linear
650 relationship between precipitation and upward moisture fluxes at lower level. The relationship

Deleted: at

19

lines from this study as shown in Fig. 13 parallel the 1:1 reference line for all resolutions. However, the lines are consistently below the reference line for the convection-permitting simulations (4km) and are above the reference line for the hydrostatic simulations with convective parameterization (e.g., 16km, 30km, 60km). The simulated precipitation can be larger than the lower level upward moisture fluxes at hydrostatic scale because part of the precipitation is contributed by the convective parameterization rather than contributed by the resolved upward moisture flux (Rauscher et al., 2016). On the contrary, precipitation could be lower than the upward moisture flux at convection-permitting scale (e.g., 4km) as moisture is removed from cloud updrafts due to detrainment (e.g., O'Brien et al., 2016). Overall, our results of the resolution-dependent updraft and precipitation are consistent with Rauscher et al. (2016) and O'Brien et al. (2016).

4. Summary and discussion

In this study, a series of MPAS simulations of a heavy precipitation event over East China, triggered by a typical southwest vortex in the middle and high troposphere and wind shear in the lower layer of the Meiyu front during the East Asian summer monsoon, are compared. The simulations are performed at various resolutions from hydrostatic (60 km, 30 km, 16 km) to non-hydrostatic (4 km) scales. Consistency between the MPAS simulations at global uniform and variable resolutions is also investigated. Besides the impacts of resolution on simulating heavy precipitation, the impacts of convective and cloud microphysics schemes are also examined. All the MPAS simulations are evaluated using the CMA station observations of precipitation and the ERA5 reanalysis of winds, and compared against the NCEP GFS forecasts that share the same initial condition of the MPAS simulations.

In general, the MPAS simulations at global uniform (U15km) and variable (V16km) resolutions produce similar results in terms of the spatial and temporal distributions of precipitation and winds inside the refined region over East China. Both experiments can capture the observed precipitation characteristics. This suggests that the global variable-resolution configuration of MPAS may be appropriate to simulate heavy precipitation over East China, which is also consistent with the finding from previous studies using variable resolution MPAS with regional refinement over other parts of the globe (e.g., Sakaguchi et al., 2015; Zhao et al., 2016). The simulations with two different convective parameterizations show that the MPAS simulated distributions of precipitation are affected by the convective schemes at hydrostatic scales, while the impacts from the cloud microphysics schemes are small.

20

The variable-resolution simulations spanning hydrostatic and non-hydrostatic scales reveal that the scale-aware GF convective parameterization produces less convective parameterized precipitation as the horizontal resolution increases. Comparison against the station observations indicates that the MPAS simulations at 16 km and 4 km can generally better capture the observed temporal and zonal distribution of the rain belt in the simulated event than the simulations at coarser resolutions. The experiments at 4 km can better capture the areas with heavy precipitation (> 50 mm/day) than the experiments at coarser resolutions compared to the observations, although the simulations at 4 km overestimate the first peak precipitation and underestimate the second one. This may indicate that the convective parameterization appears not to be able to produce intense precipitation. The analysis also shows that the underestimation of intense precipitation is consistent with the underestimation of resolved upward motions in the simulations at coarser resolutions. The biases in the locations of rain belt are mainly due to failure of the model to simulate the wind shear structure of the Meiyu front during this event. This suggests that the position and structure of the wind shear of the Meiyu front that produces the vertical motion is sensitive to the models and their specific configurations even though all simulations share the same initial condition. Previous studies have found that the formation and evolution of wind shear during the Meiyu front can interact with multiscale processes and systems over East China, including terrain and convective latent heat (Yao et al., 2017). Therefore, different representation of the terrain over East China in various resolutions and convective latent heat resulted from different physics schemes may affect the simulated wind shear structure among the MPAS experiments at various resolutions and between MPAS and GFS.

The performance of MPAS at convection-permitting scale is quite sensitive to the cloud microphysics scheme in terms of the distribution and intensity of extreme precipitation. This is consistent with Feng et al. (2018), who found that cloud microphysics parameterizations in convection permitting regional simulations have important effects on macroscale properties such as the lifetime, precipitation amount, stratiform versus convective rain volumes of mesoscale convective systems in the U.S. They attributed the impacts to the representation of ice phase hydrometeor species that influence the mesoscale convective systems through their influence on the diabatic heating profiles that provide dynamical feedback to the circulation (Yang et al. 2017). Hence more efforts may be needed to improve cloud microphysics processes for modeling extreme precipitation at convection-permitting scale in the future. In the meantime, aerosols have been found to play a critical role in simulating some heavy precipitation events over China through their impacts on cloud microphysics and/or radiation

Deleted: Further investigation of MPAS experiments at multiple resolutions from hydrostatic (60 km, 30 km, 16 km) to non-hydrostatic (4 km) scales over East China shows significant impacts of resolution on simulating the spatial distributions of precipitation and winds.

Deleted: Meanwhile, the subgrid-scale motions become increasingly resolved and the ratio of grid-scale to total precipitation increases over the refined region as resolution increases to 4 km.

Deleted: The simulations at coarser resolutions of 60 km and 30 km produce weaker precipitation and a southward shift of the rain belt. In contrast, the GFS forecasts at 0.5° and 1.0° produce a northward shift of the rain belt.

Formatted: Not Highlight

Deleted: The analysis also indicates the significant impacts from cloud microphysics on the MPAS simulations at 4 km in terms of precipitation distribution and intensity.

Deleted: The distributions of rain belt are consistent with the zonal shift of vertical motion.

Deleted: Besides the general zonal distribution of the rain belt, the distribution and intensity of heavy precipitation are also investigated. The experiments at 4 km can better capture the areas with heavy precipitation (> 50 mm/day) than the experiments at coarser resolutions compared to the observations, although the simulations at 4 km overestimate the first peak precipitation and underestimate the second one. In addition, the MPAS simulations at 4 km can better generate the frequency of intense precipitation that is significantly underestimated by simulations at coarser resolutions, which may indicate that the convective parameterization appears not to be able to produce intense precipitation. The analysis also shows that the underestimation of intense precipitation is consistent with the underestimation of resolved upward motions in the simulations at coarser resolutions. Although the MPAS simulations at 4 km generally produce better results than the experiments at coarser resolutions particularly 30 km and up, they still have some biases in the timing and intensity of precipitation. In addition, t

Formatted: Highlight

757 (e.g., Zhong et al., 2015, 2017; Fan et al., 2015). The current version of MPAS does not
758 represent aerosol-radiation and aerosol-cloud interactions, which may also contribute to the
759 biases of extreme precipitation at convection-permitting scales. Lastly, it is also noteworthy
760 that the resolution of 4 km may still be insufficient to resolve some convective cells, which
761 may also contribute to the modeling biases (Bryan and Morrison, 2012).

762 This study provides the first evidence supporting the use of global variable resolution
763 configuration of MPAS for simulating extreme precipitation events over East China. In
764 particular, the MPAS variable-resolution experiment at convection-permitting scale (4 km)
765 improves the simulated distribution and intensity of precipitation over the area of interest,
766 which is consistent with previous studies using regional convection permitting models (e.g.,
767 Zhang et al., 2013; Prein et al., 2015; Yang et al. 2017; Gao et al. 2017; Feng et al. 2018). The
768 higher resolution MPAS experiments simulate better spatial distribution of heavy precipitation
769 over the complex topographic region of East China, which suggests that topography may play
770 a critical role and deserves further investigation in the future. Our results show that cloud
771 microphysics parameterizations have important effects in convection permitting simulations,
772 but modeling of other physical processes such as boundary layer turbulence, radiation, and
773 aerosols may also affect the skill of convection permitting simulations. The GFS forecasts
774 analyzed in this study show significant biases in precipitation distribution. The zonal shift of
775 the rain belt by the MPAS simulations at coarser resolutions compared to simulations at finer
776 resolutions suggests that resolution may have contributed to the GFS forecast biases. A more
777 detailed exploration of the differences between the MPAS and GFS simulations is beyond the
778 scope of this study.

779 Previous studies (Xue et al., 2007; Clark et al. 2016) noted the importance of ensemble
780 simulations in predicting heavy precipitation. Due to the computational limitation, only one set
781 of experiments with different physics and resolutions are evaluated in this study. The MPAS
782 simulations of heavy precipitation with different initial conditions and refinement sizes deserve
783 more evaluations. Finally, some studies noted that convection-permitting modeling does not
784 always add values in simulating heavy precipitation compared to hydrostatic scale modeling
785 (e.g., Kain et al., 2008; Rhoades et al., 2018; Xu et al., 2018). Rhoades et al. (2018) found that
786 the improvement by increasing resolution may also depend on cloud microphysics
787 parameterization. Increasing horizontal resolution alone sometimes can even lead to worse
788 model performance. The impacts of increasing horizontal resolution on the overall model
789 performance in simulating extreme precipitation may also be affected by the model structure
790 and coupling among model components and processes (Jeevanjee et al., 2016; O'Brien et al.,

22

791 2016; Herrington et al., 2017, 2018; Gross et al., 2018). This study also found some sensitivity
792 of modeling extreme precipitation to cloud microphysics, particularly at convection-permitting
793 scale. More events of heavy precipitation over East China should be investigated in the future
794 to more systematically evaluate the MPAS variable-resolution modeling framework and the
795 impacts of resolution and physical parameterizations.
796
797 **Code availability**
798 The MPAS release v5.2 can be obtained at *mpas-dev.github.io*. Global meshes generated for
799 the experiments used in this study are available upon request by contacting the corresponding
800 author.
801
802 **Author contributions**
803 CZ and YW designed research. MX performed the simulations. CZ, MX, MZ, and ZH analyzed
804 the simulations. JG collected and analyzed the observations. CZ, MX, and YW wrote the paper.
805 LRL, MD, and WS guided the experiment design and edited the paper.
806

816

23

Reference

Arakawa, A., Jung, J. H., & Wu, C. M.: Toward unification of the multiscale modeling of the atmosphere. Atmospheric Chemistry and Physics, 11(8), 3731-3742. https://doi.org/10.5194/acp-11-3731-2011, 2011.

Bacmeister, J. T., Wehner, M. F., Neale, R. B., Gettelman, A., Hannay, C., Lauritzen, P. H., ... & Truesdale, J. E.: Exploratory high-resolution climate simulations using the Community Atmosphere Model (CAM). Journal of Climate, 27(9), 3073-3099. https://doi.org/10.1175/JCLI-D-13-00387.1, 2014.

Bechtold, P., Chaboureau, J. P., Beljaars, A., Betts, A. K., Köhler, M., Miller, M., & Redelsperger, J. L.: The simulation of the diurnal cycle of convective precipitation over land in a global model. Quarterly Journal of the Royal Meteorological Society, 130(604), 3119-3137. https://doi.org/10.1256/qj.03.103, 2004.

Bechtold, P., Köhler, M., Jung, T., Doblas-Reyes, F., Leutbecher, M., Rodwell, M. J., ... & Balsamo, G.: Advances in simulating atmospheric variability with the ECMWF model: From synoptic to decadal time-scales. Quarterly Journal of the Royal Meteorological Society, 134(634), 1337-1351. https://doi.org/10.1002/qj.289, 2008.

Bechtold, P., Semane, N., Lopez, P., Chaboureau, J. P., Beljaars, A., & Bormann, N.: Representing equilibrium and nonequilibrium convection in large-scale models. Journal of the Atmospheric Sciences, 71(2), 734-753. https://doi.org/10.1175/JAS-D-13-0163.1, 2014.

Bryan, G. H., and H. Morrison: Sensitivity of a simulated squall line to horizontal resolution and parameterization of microphysics. Mon. Wea. Rev., 140, 202–225, https://doi.org/10.1175/MWR-D-11-00046.1, 2012.

Burakowski, E. A., Tawfik, A., Ouimette, A., Lepine, L., Zarzycki, C., Novick, K., ... & Bonan, G.: Simulating surface energy fluxes using the variable-resolution Community Earth System Model (VR-CESM). Theoretical and Applied Climatology, 1-19. https://doi.org/10.1007/s00704-019-02785-0, 2019.

Chauvin, F., J.-F. Royer, and M. Deque: Response of hurricane type vortices to global warming as simulated by ARPEGE-Climat at high resolution. Climate Dyn., 27, 377-399, https://doi.org/10.1007/s00382-006-0135-7, 2006.

Chen, F., & Dudhia, J.: Coupling an advanced land surface–hydrology model with the Penn State–NCAR MM5 modeling system. Part I: Model implementation and

24

849   sensitivity. Monthly Weather Review, 129(4), 569-585. https://doi.org/10.1175/1520-
850   0493(2001)129<0569:CAALSH>2.0.CO;2, 2001.

851 Déqué, M., Jones, R. G., Wild, M., Giorgi, F., Christensen, J. H., Hassell, D. C., ... & De Castro,
852   M.: Global high resolution versus Limited Area Model climate change projections over
853   Europe: quantifying confidence level from PRUDENCE results. Climate
854   Dynamics, 25(6), 653-670. https://doi.org/10.1007/s00382-005-0052-1, 2005.

855 Déqué, M., & Piedelievre, J. P.: High resolution climate simulation over Europe. Climate
856   dynamics, 11(6), 321-339. https://doi.org/10.1007/BF00215735, 1995.

857 Déqué, M., Rowell, D. P., Lüthi, D., Giorgi, F., Christensen, J. H., Rockel, B., ... & van den
858   Hurk, B. J. J. M.: An intercomparison of regional climate simulations for Europe:
859   assessing uncertainties in model projections. Climatic Change, 81(1), 53-70.
860   https://doi.org/10.1007/s10584-006-9228-x, 2007.

861 Ding, Y., Wang, Z., & Sun, Y.: Inter‐decadal variation of the summer precipitation in East
862   China and its association with decreasing Asian summer monsoon. Part I: Observed
863   evidences. International Journal of Climatology, 28(9), 1139-1161.
864   https://doi.org/10.1002/joc.1615, 2008.

865 Clark, P., Roberts, N., Lean, H., Ballard, S. P., & Charlton‐Perez, C.: Convection‐permitting
866   models: a step‐change in rainfall forecasting. Meteorological Applications, 23(2), 165-
867   181. https://doi.org/10.1002/met.1538, 2016.

868 Du, Q., Faber, V., & Gunzburger, M.: Centroidal Voronoi tessellations: Applications and
869   algorithms. SIAM review, 41(4), 637-676.
870   https://doi.org/10.1137/S0036144599352836, 1999.

871 ECMWF: ECMWF strategy 2016–2025: The strength of a common goal. European Centre for
872   Medium-Range Weather Forecasts Tech. Rep., 32
873   pp.https://www.ecmwf.int/sites/default/files/ECMWF_Strategy_2016-2025.pdf, 2016.

874 Efron, B.: Bootstrap methods: another look at the jackknife. In Breakthroughs in statistics (pp.
875   569-593). Springer, New York, NY. https://doi.org/10.1007/978-1-4612-4380-9_41,
876   1992.

877 Efron, B., & Tibshirani, R. J.: An introduction to the bootstrap. CRC press, 1994.

878 Fan, J., Rosenfeld, D., Yang, Y., Zhao, C., Leung, L. R., & Li, Z.: Substantial contribution of
879   anthropogenic air pollution to catastrophic floods in Southwest China. Geophysical
880   Research Letters, 42(14), 6066-6075. https://doi.org/10.1002/2015GL064479, 2015.

881 Feng, Z., L.R. Leung, R.A. Houze, Jr., S. Hagos, J. Hardin, Q. Yang. B. Han, & J. Fan:
882   Structure and evolution of mesoscale convective systems: sensitivity to cloud
883   microphysics in convection-permitting simulations over the U.S. J. Adv. Model. Earth
884   Syst., 10, https://doi.org/10.1029/2018MS001305, 2018.

885 Fowler, L. D., Skamarock, W. C., Grell, G. A., Freitas, S. R., & Duda, M. G.: Analyzing the
886   Grell–Freitas convection scheme from hydrostatic to nonhydrostatic scales within a
887   global model. Monthly Weather Review, 144(6), 2285-2306.
888   https://doi.org/10.1175/MWR-D-15-0311.1, 2016.

889 Fritsch, J. M., & Carbone, R. E.: Improving quantitative precipitation forecasts in the warm
890   season: A USWRP research and development strategy. Bulletin of the American
891   Meteorological Society, 85(7), 955-966. https://doi.org/10.1175/BAMS-85-7-955,
892   2004.

893 Gao, Y., L.R. Leung, C. Zhao, & S. Hagos: Sensitivity of summer precipitation to model
894   resolution and convective parameterizations across gray zone resolutions. J. Geophys.
895   Res., 122, 2714-2733, doi:10.1002/2016JD025896, 2017.

896 Gettelman, A., Callaghan, P., Larson, V. E., Zarzycki, C. M., Bacmeister, J. T., Lauritzen, P.
897   H., ... & Neale, R. B.: Regional climate simulations with the community earth system
898   model. Journal of Advances in Modeling Earth Systems, 10(6), 1245-1265.
899   https://doi.org/10.1002/2017MS001227, 2018.

900 Gettelman A., Morrison H., Thompson G.: Cloud Microphysics Across Scales for Weather and
901   Climate. In: Randall D., Srinivasan J., Nanjundiah R., Mukhopadhyay P. (eds) Current
902   Trends in the Representation of Physical Processes in Weather andClimate Models.
903   Springer Atmospheric Sciences. Springer, Singapore, 2019.

904 Giorgi, F., and Marinucci, M. R.: A investigation of the sensitivity of simulated precipitation
905   to model resolution and its implications for climate studies. Monthly Weather
906   Review, 124(1), 148-166. https://doi.org/10.1175/1520-
907   0493(1996)124<0148:AIOTSO>2.0.CO;2, 1996.

908 Giorgi, F., and Mearns, L. O.: Approaches to the simulation of regional climate change: a
909   review. Reviews of Geophysics, 29(2), 191-216. https://doi.org/10.1029/90RG02636,
910   1991.

911 Grell, G. A., & Dévényi, D.: A generalized approach to parameterizing convection combining
912   ensemble and data assimilation techniques. Geophysical Research Letters, 29(14), 38-
913   1. https://doi.org/10.1029/2002GL015311, 2002.

914 Grell, G. A., & Freitas, S. R.: A scale and aerosol aware stochastic convective parameterization
915   for weather and air quality modeling. Atmos. Chem. Phys, 14(10), 5233-5250.
916   https://doi.org/10.5194/acp-14-5233-2014, 2014.

917 Gross, M., Wan, H., Rasch, P. J., Caldwell, P. M., Williamson, D. L., Klocke, D., Christiane,
918   J, Diana, T., Nigel, W., Mike, C, Bob, B., Martin, W., Florian, L., Eric, B., Sylvie, M.,
919   Piet, T., Almut, G., Peter, L., Hans, J., Colin, Z., Sakaguchi, K., Leung, R.: Physics–
920   Dynamics Coupling in Weather, Climate, and Earth System Models: Challenges and
921   Recent Progress. Monthly Weather Review, 146(11), 3505-3544.
922   https://doi.org/10.1175/MWR-D-17-0345.1, 2018.

923 Guo, J., Su, T., Li, Z., Miao, Y., Li, J., Liu, H., Xu, H., Cribb, M., and Zhai, P.: Declining
924   frequency of summertime local-scale precipitation over eastern China from 1970 to
925   2010 and its potential link to aerosols. Geophysical Research Letters, 44(11), 5700-
926   5708, 2017.

927 Hagos, S., Leung, L. R., Yang, Q., Zhao, C., and Lu, J.: Resolution and dynamical core
928   dependence of atmospheric river frequency in global model simulations. Journal of
929   Climate, 28(7), 2764-2776. https://doi.org/10.1175/JCLI-D-14-00567.1, 2015.

930 Herrington, A. R., & Reed, K. A.: An explanation for the sensitivity of the mean state of the
931   community atmosphere model to horizontal resolution on aquaplanets. Journal of
932   Climate, 30(13), 4781-4797. https://doi.org/10.1175/JCLI-D-16-0069.1, 2017.

933 Herrington, A. R., & Reed, K. A.: An Idealized Test of the Response of the Community
934   Atmosphere Model to Near - Grid - Scale Forcing Across Hydrostatic
935   Resolutions. Journal of Advances in Modeling Earth Systems, 10(2), 560-575.
936   https://doi.org/10.1002/2017MS001078, 2018.

937 Fildier, B., Parishani, H., & Collins, W. D.: Prognostic Power of Extreme Rainfall Scaling
938   Formulas Across Space and Time Scales. Journal of Advances in Modeling Earth
939   Systems, 10(12), 3252-3267. https://doi.org/10.1029/2018MS001462, 2018.

940 Hong, S. Y.: A new stable boundary - layer mixing scheme and its impact on the simulated East
941   Asian summer monsoon. Quarterly Journal of the Royal Meteorological
942   Society, 136(651), 1481-1496. https://doi.org/10.1002/qj.665, 2010.

943 Hong, S. Y., & Lim, J. O. J.: The WRF single-moment 6-class microphysics scheme
944   (WSM6). J. Korean Meteor. Soc, 42(2), 129-151, 2006.

Hong, S. Y., Noh, Y., & Dudhia, J.: A new vertical diffusion package with an explicit treatment of entrainment processes. Monthly weather review, 134(9), 2318-2341. https://doi.org/10.1175/MWR3199.1, 2006.

Huang, X., Rhoades, A. M., Ullrich, P. A., & Zarzycki, C. M.: An evaluation of the variable-resolution CESM for modeling California's climate. Journal of Advances in Modeling Earth Systems, 8(1), 345-369. https://doi.org/10.1002/2015MS000559, 2016.

Hui, P., Tang, J., Wang, S., & Wu, J.: Sensitivity of simulated extreme precipitation and temperature to convective parameterization using RegCM3 in China. Theoretical and applied climatology, 122(1-2), 315-335. https://doi.org/10.1007/s00704-014-1300-2, 2015.

Iacono, M. J., Mlawer, E. J., Clough, S. A., & Morcrette, J. J.: Impact of an improved longwave radiation model, RRTM, on the energy budget and thermodynamic properties of the NCAR community climate model, CCM3. Journal of Geophysical Research: Atmospheres, 105(D11), 14873-14890. https://doi.org/10.1029/2000JD900091, 2000.

Jeevanjee, N.: Vertical velocity in the gray zone. Journal of Advances in Modeling Earth Systems, 9(6), 2304-2316. https://doi.org/10.1002/2017MS001059, 2017.

Judt, F.: Insights into Atmospheric Predictability through Global Convection-Permitting Model Simulations. Journal of the Atmospheric Sciences, 75(5), 1477-1497. https://doi.org/10.1175/JAS-D-17-0343.1, 2018.

Ju, L., Ringler, T., & Gunzburger, M.: Voronoi tessellations and their application to climate and global modeling. In Numerical techniques for global atmospheric models (pp. 313-342). Springer, Berlin, Heidelberg. https://doi.org/10.1007/978-3-642-11640-7_10, 2011.

Kain, J. S.: The Kain–Fritsch convective parameterization: an update. Journal of applied meteorology, 43(1), 170-181. https://doi.org/10.1175/1520-0450(2004)043<0170:TKCPAU>2.0.CO;2, 2004.

Kain, J. S., Weiss, S. J., Bright, D. R., Baldwin, M. E., Levit, J. J., Carbin, G. W., ... & Thomas, K. W.: Some practical considerations regarding horizontal resolution in the first generation of operational convection-allowing NWP. Weather and Forecasting, 23(5), 931-952. https://doi.org/10.1175/WAF2007106.1, 2008.

Klemp, J. B.: A terrain-following coordinate with smoothed coordinate surfaces. Monthly weather review, 139(7), 2163-2169. https://doi.org/10.1175/MWR-D-10-05046.1, 2011.

978   Klemp, J. B., Skamarock, W. C., & Dudhia, J.: Conservative split-explicit time integration
979   methods for the compressible nonhydrostatic equations. Monthly Weather
980   Review, 135(8), 2897-2913. https://doi.org/10.1175/MWR3440.1, 2007.
981   Landu, K., Leung, L. R., Hagos, S., Vinoj, V., Rauscher, S. A., Ringler, T., & Taylor, M.: The
982   dependence of ITCZ structure on model resolution and dynamical core in aquaplanet
983   simulations. Journal of Climate, 27(6), 2375-2385. https://doi.org/10.1175/JCLI-D-13-
984   00269.1, 2014.
985   Laprise, R.: Regional climate modelling. Journal of Computational Physics, 227(7), 3641-3666.
986   https://doi.org/10.1016/j.jcp.2006.10.024, 2008.
987   Leung, L. R., & Qian, Y.: The sensitivity of precipitation and snowpack simulations to model
988   resolution via nesting in regions of complex terrain. Journal of Hydrometeorology, 4(6),
989   1025-1043.   https://doi.org/10.1175/1525-7541(2003)004<1025:TSOPAS>2.0.CO;2,
990   2003.
991   Leung, L. R., Ringler, T., Collins, W. D., Taylor, M., & Ashfaq, M.: A hierarchical evaluation
992   of regional climate simulations. Eos, Transactions American Geophysical
993   Union, 94(34), 297-298. https://doi.org/10.1002/2013EO340001, 2013.
994   Li, J., Zhang, Q., Chen, Y. D., & Singh, V. P.: GCMssimulations. Eos, Transactions American
995   Ge extremes during the 21st century in China. Journal of Geophysical Research:
996   Atmospheres, 118(19). https://doi.org/10.1002/jgrd.50851, 2013.
997   Li, W., Jiang, Z., Xu, J., & Li, L.: Extreme Precipitation Indices over China in CMIP5 Models.
998   Part   II: Probabilistic   Projection. Journal   of   Climate, 29(24),   8989-9004.
999   https://doi.org/10.1175/JCLI-D-16-0377.1, 2016.
1000 Li, Z., W. K.-M. Lau, V. Ramanathan et al.: Aerosol and monsoon climate interactions over
1001   Asia, *Rev. Geophys.*, 54, https://doi.org/10.1002/2015RG000500, 2016.
1002 Lin, Z., & Wang, B.: Northern East Asian low and its impact on the interannual variation of
1003   East   Asian   summer   rainfall. Climate   dynamics, 46(1-2),   83-97.
1004   https://doi.org/10.1007/s00382-015-2570-9, 2016.
1005 Liu, R., Liu, S. C., Cicerone, R. J., Shiu, C. J., Li, J., Wang, J., & Zhang, Y.: Trends of extreme
1006   precipitation in eastern China and their possible causes. Advances in Atmospheric
1007   Sciences, 32(8), 1027-1037. https://doi.org/10.1007/s00376-015-5002-, 2015.
1008 Locatelli, J. D., & Hobbs, P. V.: Fall speeds and masses of solid precipitation particles. Journal
1009   of   Geophysical   Research,   79(15),   2185-2197.
1010   https://doi.org/10.1029/JC079i015p02185, 1974.

29

1011 Lorant, V., & Royer, J. F.: Sensitivity of equatorial convection to horizontal resolution in
1012   aquaplanet simulations with a variable-resolution GCM. Monthly weather
1013   review, 129(11), 2730-2745. https://doi.org/10.1175/1520-
1014   0493(2001)129<2730:SOECTH>2.0.CO;2, 2001.

1015 Lu, J., Chen, G., Leung, L. R., Burrows, D. A., Yang, Q., Sakaguchi, K., & Hagos, S.: Toward
1016   the dynamical convergence on the jet stream in aquaplanet AGCMs. Journal of
1017   Climate, 28(17), 6763-6782. https://doi.org/10.1175/JCLI-D-14-00761.1, 2015.

1018 Mlawer, E. J., Taubman, S. J., Brown, P. D., Iacono, M. J., & Clough, S. A.: Radiative transfer
1019   for inhomogeneous atmospheres: RRTM, a validated correlated‐k model for the
1020   longwave. Journal of Geophysical Research: Atmospheres, 102(D14), 16663-16682.
1021   https://doi.org/10.1029/97JD00237., 1997.

1022 Molthan, A. L., & Colle, B. A.: Comparisons of single-and double-moment microphysics
1023   schemes in the simulation of a synoptic-scale snowfall event. Monthly Weather Review,
1024   140(9), 2982-3002. https://doi.org/10.1175/MWR-D-11-00292.1, 2012.

1025 Nakanishi, M., & Niino, H.: An improved Mellor–Yamada level-3 model: Its numerical
1026   stability and application to a regional prediction of advection fog. Boundary-Layer
1027   Meteorology, 119(2), 397-407. https://doi.org/10.1007/s10546-005-9030-8, 2006.

1028 Nakanishi, M., & Niino, H.: Development of an improved turbulence closure model for the
1029   atmospheric boundary layer. Journal of the Meteorological Society of Japan. Ser.
1030   II, 87(5), 895-912. https://doi.org/10.2151/jmsj.87.895, 2009.

1031 NRC: National Research Council Board, A National Strategy for Advancing Climate Modeli
1032   ng, The National Academies Press, Washington, DC (2012) (http://www.nap.edu/cata
1033   log/13430/a-national-strategy-for-advancing-climate-
1034   modeling, last access: April 25, 2019).

1035 O'Brien, T. A., Collins, W. D., Kashinath, K., Rübel, O., Byna, S., Gu, J., Krishnan, H, Ullrich,
1036   P.: Resolution dependence of precipitation statistical fidelity in hindcast
1037   simulations. Journal of Advances in Modeling Earth Systems, 8(2), 976-990.
1038   https://doi.org/10.1002/2016MS000671, 2016.

1039 O'Brien, T. A., Li, F., Collins, W. D., Rauscher, S. A., Ringler, T. D., Taylor, M., Hagos, S.
1040   M., Leung, L. R.: Observed scaling in clouds and precipitation and scale incognizance
1041   in regional to global atmospheric models. Journal of Climate, 26(23), 9313-9333.
1042   https://doi.org/10.1175/JCLI-D-13-00005.1, 2013.

Park, S. H., Skamarock, W. C., Klemp, J. B., Fowler, L. D., & Duda, M. G.: Evaluation of global atmospheric solvers using extensions of the Jablonowski and Williamson baroclinic wave test case. Monthly Weather Review, 141(9), 3116-3129. https://doi.org/10.1175/MWR-D-12-00096.1, 2013.

Pedersen, C. A., & Winther, J. G.: Intercomparison and validation of snow albedo parameterization schemes in climate models. Climate Dynamics, 25(4), 351-362: https://doi.org/10.1007/s00382-005-0037-0, 2005.

Prein, A. F., Langhans, W., Fosser, G., Ferrone, A., Ban, N., Goergen, K., ... & Brisson, E.: A review on regional convection - permitting climate modeling: Demonstrations, prospects, and challenges. Reviews of geophysics, 53(2), 323-361. https://doi.org/10.1002/2014RG000475, 2015.

Prein, A. F., Rasmussen, R. M., Ikeda, K., Liu, C., Clark, M. P., & Holland, G. J.: The future intensification of hourly precipitation extremes. Nature Climate Change, 7(1), 48. https://doi.org/10.1038/nclimate3168, 2017.

Rauscher, S. A., O'Brien, T. A., Piani, C., Coppola, E., Giorgi, F., Collins, W. D., & Lawston, P. M.: A multimodel intercomparison of resolution effects on precipitation: simulations and theory. Climate dynamics, 47(7-8), 2205-2218. https://doi.org/10.1007/s00382-015-2959-5, 2016.

Rauscher, S. A., Ringler, T. D., Skamarock, W. C., & Mirin, A. A.: Exploring a global multiresolution modeling approach using aquaplanet simulations. Journal of Climate, 26(8), 2432-2452. https://doi.org/10.1175/JCLI-D-12-00154.1, 2013.

Rhoades, A. M., Huang, X., Ullrich, P. A., & Zarzycki, C. M.: Characterizing Sierra Nevada snowpack using variable-resolution CESM. Journal of Applied Meteorology and Climatology, 55(1), 173-196. https://doi.org/10.1175/JAMC-D-15-0156.1, 2016.

Rhoades, A. M., Ullrich, P. A., Zarzycki, C. M., Johansen, H., Margulis, S. A., Morrison, H., ... & Collins, W. D.: Sensitivity of Mountain Hydroclimate Simulations in Variable - Resolution CESM to Microphysics and Horizontal Resolution. Journal of Advances in Modeling Earth Systems, 10(6), 1357-1380. https://doi.org/10.1029/2018MS001326, 2018.

Ringler, T. D., Jacobsen, D., Gunzburger, M., Ju, L., Duda, M., & Skamarock, W.: Exploring a multiresolution modeling approach within the shallow-water equations. Monthly Weather Review, 139(11), 3348-3368. https://doi.org/10.1175/MWR-D-10-05049.1, 2011.

1076 Ringler, T., Ju, L., & Gunzburger, M.: A multiresolution method for climate system modeling:
1077   Application of spherical centroidal Voronoi tessellations. Ocean Dynamics, 58(5-6),
1078   475-498. https://doi.org/10.1007/s10236-008-0157-2, 2008.

1079 Sakaguchi, K., Leung, L. R., Zhao, C., Yang, Q., Lu, J., Hagos, S.: Exploring a multiresolution
1080   approach using AMIP simulations. Journal of Climate, 28(14), 5549-5574.
1081   https://doi.org/10.1175/JCLI-D-14-00729.1, 2015.

1082 Sakaguchi, K., Lu, J., Leung, L. R., Zhao, C., Li, Y., & Hagos, S.: Sources and pathways of
1083   the   upscale   effects   on   the   Southern   Hemisphere   jet   in
1084   MPASs. s. ions. s. ons. ultiresolution approach using AMIP simulations. lations. nd
1085   Williams25-10431043 4(6https://doi.org/10.1002/2016MS000743, 2016.

1086 Skamarock, W. C., & Gassmann, A.: Conservative transport schemes for spherical geodesic
1087   grids: High-order flux operators for ODE-based time integration. Monthly Weather
1088   Review, 139(9), 2962-2975. https://doi.org/10.1175/MWR-D-10-05056.1, 2011.

1089 Skamarock, W. C., & Klemp, J. B.: A time-split nonhydrostatic atmospheric model for weather
1090   research and forecasting applications. Journal of Computational Physics, 227(7), 3465-
1091   3485. https://doi.org/10.1016/j.jcp.2007.01.037, 2008.

1092 Skamarock, W. C., Klemp, J. B., Duda, M. G., Fowler, L. D., Park, S. H., & Ringler, T. D.: A
1093   multiscale nonhydrostatic atmospheric model using centroidal Voronoi tesselations and
1094   C-grid   staggering. Monthly   Weather   Review, 140(9),   3090-3105.
1095   https://doi.org/10.1175/MWR-D-11-00215.1, 2012.

1096 Sukovich, E. M., Ralph, F. M., Barthold, F. E., Reynolds, D. W., & Novak, D. R.: Extreme
1097   quantitative precipitation forecast performance at the Weather Prediction Center from
1098   2001 to 2011. Weather and Forecasting, 29(4), 894-911. https://doi.org/10.1175/WAF-
1099   D-13-00061.1, 2014.

1100 Thompson, G., Field, P. R., Rasmussen, R. M., & Hall, W. D.: Explicit forecasts of winter
1101   precipitation using an improved bulk microphysics scheme. Part II: Implementation of
1102   a new snow parameterization. Monthly Weather Review, 136(12), 5095-5115.
1103   https://doi.org/10.1175/2008MWR2387.1, 2008.

1104 Wang, M., & Ullrich, P.: Marine air penetration in California's Central Valley: Meteorological
1105   drivers and the impact of climate change. Journal of Applied Meteorology and
1106   Climatology, 57(1), 137-154. https://doi.org/10.1175/JAMC-D-17-0089.1, 2018.

1107 Wang, Y., Leung, L. R., McGREGOR, J. L., Lee, D. K., Wang, W. C., Ding, Y., & Kimura,
1108   F.: Regional climate modeling: progress, challenges, and prospects. Journal of the

1109   Meteorological   Society   of   Japan.   Ser.   II, 82(6),   1599-1628.
1110   https://doi.org/10.2151/jmsj.82.1599, 2004.

1111   Wicker, L. J., & Skamarock, W. C.: Time-splitting methods for elastic models using forward
1112   time   schemes. Monthly   weather   review, 130(8),   2088-2097.
1113   https://doi.org/10.1175/1520-0493(2002)130<2088:TSMFEM>2.0.CO;2, 2002.

1114   Wu, C., Liu, X., Lin, Z., Rhoades, A. M., Ullrich, P. A., Zarzycki, C. M., ... & Rahimi-Esfarjani,
1115   S. R.: Exploring a variable-resolution approach for simulating regional climate in the
1116   Rocky Mountain region using the VR-CESM. Journal of Geophysical Research:
1117   Atmospheres, 122(20), 10-939. https://doi.org/10.1002/2017JD027008, 2017.

1118   Xiang, S., Li, Y., Li, D., & Yang, S.: An analysis of heavy precipitation caused by a retracing
1119   plateau vortex based on TRMM data. Meteorology and Atmospheric Physics, 122(1-2),
1120   33-45. https://doi.org/10.1007/s00703-013-0269-1, 2013.

1121   Xu, H., & Yao, W.: A numerical study of the Beijing extreme rainfall of 21 July 2012 and the
1122   impact   of   topography. Advances   in   Meteorology, 2015.
1123   http://dx.doi.org/10.1155/2015/980747, 2015.

1124   Xue, M., Kong, F., Weber, D., Thomas, K. W., Wang, Y., Brewster, K., ... & Coniglio, M. C.:
1125   CAPS realtime storm-scale ensemble and high-resolution forecasts as part of the
1126   NOAA Hazardous Weather Testbed 2007 spring experiment. In 22nd Conf. Wea. Anal.
1127   Forecasting/18th Conf. Num. Wea. Pred, 2007.

1128   Xu, Z., Rhoades, A. M., Johansen, H., Ullrich, P. A., & Collins, W. D.: An intercomparison of
1129   GCM and RCM dynamical downscaling for characterizing the hydroclimatology of
1130   California   and   Nevada. Journal   of   Hydrometeorology, 19(9),   1485-1506.
1131   https://doi.org/10.1175/JHM-D-17-0181.1, 2018.

1132   Yang, Q., Leung, L. R., Rauscher, S. A., Ringler, T. D., & Taylor, M. A.: Atmospheric moisture
1133   budget and spatial resolution dependence of precipitation extremes in aquaplanet
1134   simulations. Journal of Climate, 27(10), 3565-3581. https://doi.org/10.1175/JCLI-D-
1135   13-00468.1, 2014.

1136   Yang, Q., R. Houze, Jr., L.R. Leung, & Z. Feng : Environments of long-lived mesoscale
1137   convective systems over the Central United States in convection permitting climate
1138   simulations. J. Geophys. Res., 122, https://doi.org/10.1002/2017JD027033, 2017.

1139   Yao, X. P., Sun, J. Y., & Ma J. L.: Advances on research of Yangtze-Huaihe shear line. Plateau
1140   Meteorology, 36(4), 1138-1151 (in Chinese), 2017.

Yessad, K., & Bénard, P.: Introduction of a local mapping factor in the spectral part of the Météo-France global variable mesh numerical forecast model. Quarterly Journal of the Royal Meteorological Society, 122(535), 1701-1719. https://doi.org/10.1002/qj.49712253511, 1996.

Zarzycki, C. M., Jablonowski, C., & Taylor, M. A.: Using variable resolution meshes to model tropical cyclones in the community atmosphere model. Monthly Weather Review, 142(3), 1221–1239. https://doi.org/10.1175/MWR-D-13-00179.1, 2014.

Zarzycki CM, Jablonowski C, Thatcher DR, Taylor MA: Effects of localized grid refinement on the general circulation and climatology in the community atmosphere model. J Clim 28:2777–2803. https://doi.org/10.1175/JCLI-D-14-00599.1, 2015.

Zhang, D. L., Lin, Y., Zhao, P., Yu, X., Wang, S., Kang, H., & Ding, Y.: The Beijing extreme rainfall of 21 July 2012:"Right results" but for wrong reasons. Geophysical Research Letters, 40(7), 1426-1431. https://doi.org/10.1002/grl.50304, 2013.

Zhang, H., & Zhai, P.: Temporal and spatial characteristics of extreme hourly precipitation over eastern China in the warm season. Advances in atmospheric sciences, 28(5), 1177. https://doi.org/10.1007/s00376-011-0020-0, 2011.

Zhang, L., Dong, M., & Wu, T.: Changes in precipitation extremes over eastern China simulated by the Beijing Climate Center Climate System Model (BCC_CSM1. 0). Climate Research, 50(2-3), 227-245. https://doi.org/10.3354/cr01066, 2011.

Zhang, Q., Xiao, M., Singh, V. P., Liu, L., & Xu, C. Y.: Observational evidence of summer precipitation deficit-temperature coupling in China. Journal of Geophysical Research: Atmospheres, 120(19). https://doi.org/10.1002/2015JD023830, 2011.

Zhang, Q., Zheng, Y., Singh, V. P., Luo, M., & Xie, Z.: Summer extreme precipitation in eastern China: Mechanisms and impacts. Journal of Geophysical Research: Atmospheres, 122(5), 2766-2778. https://doi.org/10.1002/2016JD025913, 2017.

Zhang,Y., P., L., & Zhong, Q.: An interdecadal change in the relationship between the western North Pacific Ocean and the East Asian summer monsoon. Climate Dynamics, 49(4), 1139-1156. https://doi.org/10.1007/s00382-016-3370-6, 2017.

Zhai, P., Zhang, X., Wan, H., & Pan, X.: Trends in total precipitation and frequency of daily precipitation extremes over China. Journal of Climate, 18(7), 1096-1108. https://doi.org/10.1175/JCLI-3318.1, 2005.

Zhao, C., Leung, L. R., Park, S. H., Hagos, S., Lu, J., Sakaguchi, K., ... & Duda, M. G.: Exploring the impacts of physics and resolution on aqua,planet simulations from a

1174   nonhydrostatic global variablemresolution modeling framework. Journal of Advances
1175   in Modeling Earth Systems, 8(4), 1751-1768. https://doi.org/10.1002/2016MS000727,
1176   2017.
1177 Zhao, Y., Xu, X., Zhao, T., Xu, H., Mao, F., Sun, H., & Wang, Y.: Extreme precipitation events
1178   in East China and associated moisture transport pathways. Science China Earth
1179   Sciences, 59(9), 1854-1872. https://doi.org/10.1007/s11430-016-5315-7, 2016.
1180 Zheng, Y., Xue, M., Li, B., Chen, J., & Tao, Z.: Spatial characteristics of extreme rainfall over
1181   China with hourly through 24-hour accumulation periods based on national-level
1182   hourly rain gauge data. Advances in Atmospheric Sciences, 33(11), 1218-1232.
1183   https://doi.org/10.1007/s00376-016-6128-5, 2016.
1184 Zhong, S., pQian, Y., Zhao, C., Leung, R., & Yang, X. Q.: A case study of urbanization impact
1185   on summer preciitation in the Greater Beijing Metropolitan Area: Urban heat island
1186   versus aerosol effects. Journal of Geophysical Research: Atmospheres, 120(20), 10-
1187   903. https://doi.org/10.1002/2015JD023753, 2015.
1188 Zhong, S., Qian, Y., Zhao, C., Leung, R., Wang, H., Yang, B., ... & Liu, D.: Urbanization-
1189   induced urban heat island and aerosol effects on climate extremes in the Yangtze River
1190   Delta region of China. Atmospheric Chemistry and Physics, 17(8), 5439-5457.
1191   https://doi.org/10.5194/acp-17-5439-2017, 2017.
1192 Zhou, T. J., & Li, Z.: Simulation of the East Asian summer monsoon using a variable resolution
1193   atmospheric GCM. Climate Dynamics, 19(2), 167-180.
1194   https://doi.org/10.1007/s00382-001-0214-8, 2002.
1195
1196
1197

Table 1 Numerical Experiments conducted and analyzed in this study

Physics/Resolution	MPAS				
	U15km	U60km	V30km	V16km	V4km
WSM6+NTD	Yes	/	/	Yes	/
WSM6+GF	Yes	Yes	Yes	Yes	Yes
Thompson+GF	/	/	/	/	Yes

(1) 'U' and 'V' represent quasi-uniform and variable resolution meshes, respectively, as described in the Section 2.1.2.

(2) 'WSM6' and 'Thompson' represent two cloud microphysics schemes as described in the Section 2.1.1; 'NTD' and 'GF' represent two cumulus parameterizations as described in the Section 2.1.1.

Table 2 The mean bias (MB) and root mean square root (RMSE) of the simulated results shown in Fig. 6-8, 10 against CMA observations

	GFS.1deg		GFS.0.5deg		U60km.WSM6		V30km.WSM6		V16km.WSM6		V4km.WSM6		V4km.Thompson	
	RMSE	MB	RMSE	MB	RMSE	MB	RMSE	MB	RMSE	MB	RMSE	MB	RMSE	MB
Fig.6 [mm/day]	18.48	1.08	19.62	1.65	14.98	1.99	18.83	5.11	16.80	3.81	14.17	0.59	17.57	3.70
Fig.7 [mm/day]	18.10	0.70	18.79	1.73	9.67	2.18	10.10	3.70	6.31	2.56	3.34	0.31	13.61	5.50
Fig.8 [mm/hour]	1.17	0.06	1.21	0.10	0.78	0.12	0.86	0.18	0.74	0.14	0.83	0.04	1.22	0.26
Fig.10 [mm/day]	/	/	/	/	21.98	-0.49	28.13	7.43	24.27	3.74	21.25	2.28	25.66	6.48

Table 3 The correlation coefficients and the corresponding 95% confidence intervals based on the bootstrap analysis for the results shown in Fig. 6-10

	GFS.1deg	GFS.0.5deg	U60km.WSM6	V30km.WSM6	V16km.WSM6	V4km.WSM6	V4km.Thompson
Fig. 6	0.06 (0.006~0.1)	0.03 (-0.01~0.08)	0.49 (0.45~0.54)	0.47 (0.43~0.53)	0.56 (0.50~0.61)	0.63 (0.54~0.67)	0.54 (0.48~0.59)
Fig. 7	-0.15 (-0.35~0.24)	-0.19 (-0.39~0.15)	0.68 (0.49~0.84)	0.71 (0.46~0.88)	0.89 (0.78~0.95)	0.97 (0.93~0.99)	0.72 (0.45~0.93)
Fig. 8	0.03 (-0.02~0.09)	0.02 (-0.03~0.08)	0.30 (0.25~0.37)	0.32 (0.27~0.41)	0.41 (0.37~0.48)	0.42 (0.39~0.49)	0.38 (0.32~0.44)
Fig. 9	0.32 (0.23~0.41)	0.29 (0.20~0.41)	0.53 (0.45~0.61)	0.68 (0.64~0.72)	0.80 (0.77~0.83)	0.85 (0.82~0.88)	0.80 (0.75~0.84)
Fig. 10	/	/	0.20 (0.13~0.28)	0.21 (0.12~0.30)	0.30 (0.19~0.40)	0.50 (0.39~0.59)	0.42 (0.34~0.51)

(1) The values inside the parenthesis indicate the lower and higher bounds of 95% confidence intervals; the values outside are estimated directly based on the results shown in Fig. 6-10.

(a)

(b)

(c)

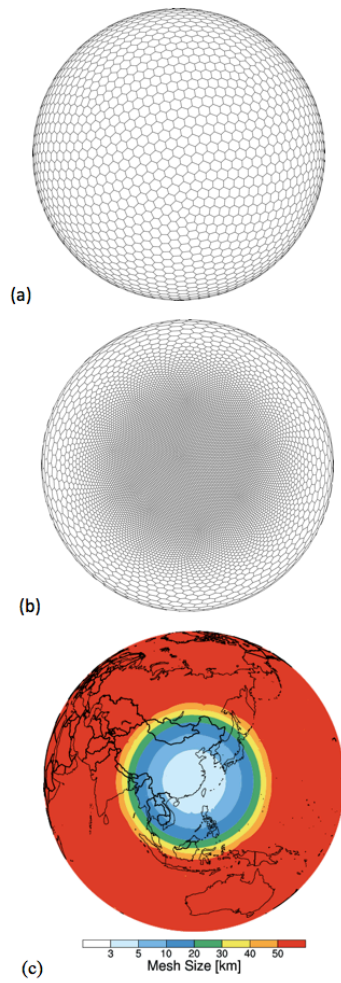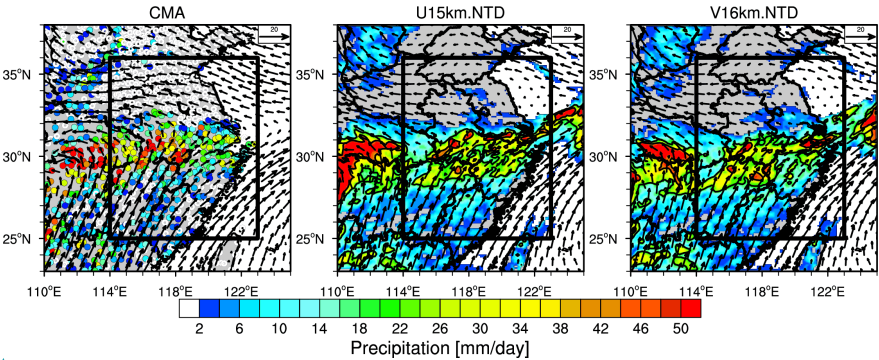Mesh Size [km]
3   5   10   20   30   40   50

Figure 1 (a) quasi-uniform mesh and (b) variable-resolution mesh used in the MPAS experiments. Both meshes are plotted at resolutions significantly lower than used in the experiments to show the mesh cells. (c) global variable-resolution mesh size distribution in the variable resolution 4-60 km experiment.

Figure 2 Spatial distributions of precipitation and wind fields at 850 hPa averaged during the event (June 25 00:00 to June 27 12:00 UTC time) from the simulations with the global uniform (15 km) and variable (16 km over the refined region as shown in Fig. 1c) resolutions. The observed mean precipitation from the CMA stations and the wind fields from the ERA5 reanalysis are shown. The black contour lines represent the precipitation larger than 20 mm/day. The black box denotes the region of East China (25°N-36°N, 114°E-123°E) for the analysis in the following.

1238
1239
1240
1241
1242
1243
1244
1245
1246
1247
1248
1249
1250
1251
1252
1253
1254
1255
1256
1257

1258
1259
1260
1261
1262
1263
1264
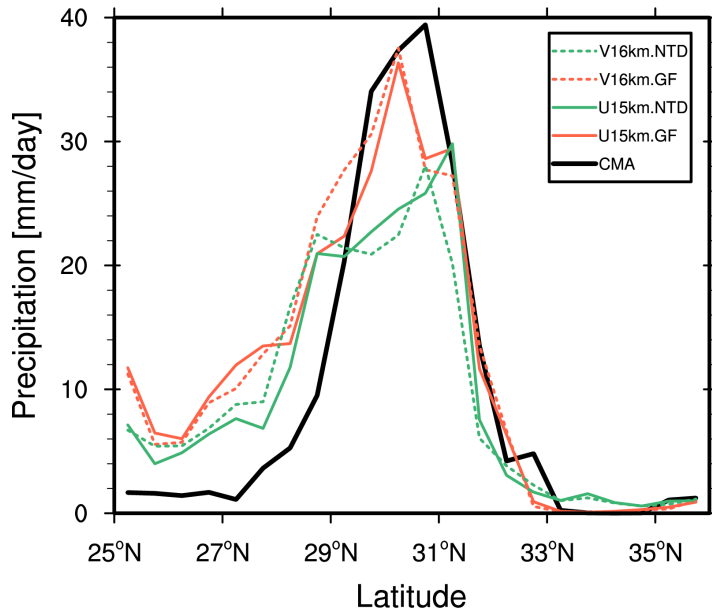
Figure 3 Zonal distributions of precipitation averaged during the event (June 25 00:00 to June
27 12:00 UTC time) <u>averaged</u> over East China (denoted as the black box in Fig. 2) from the
CMA station observations and the simulations with the global uniform (15 km, solid lines) and
variable (16 km over the refined region as shown in Fig. 1c, dash lines) resolutions with two
convective parameterizations (GF, red lines; NTD, green lines). The modeling results are
sampled at the CMA station.

1277
1278
1279
1280
1281
1282
1283
1284
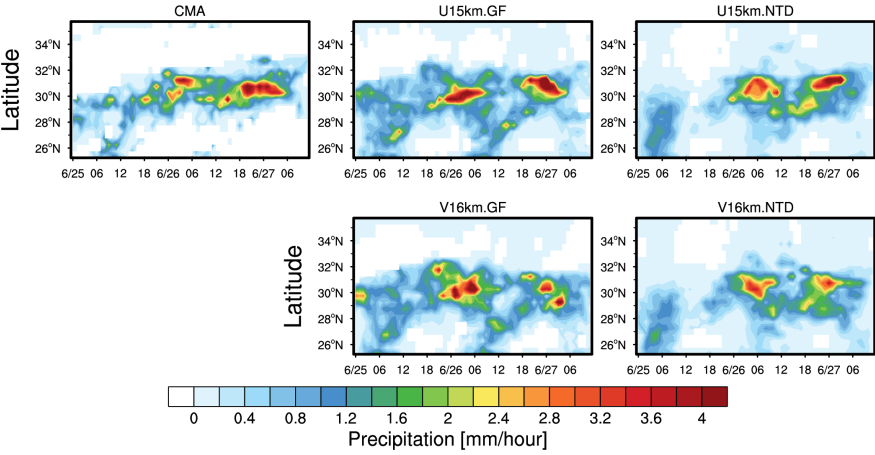
Figure 4 Time-Latitude cross section of precipitation during the event averaged over East China (denoted as the black box in Fig. 2) from the CMA station observations and the simulations with the global uniform and variable resolutions with two convective parameterizations. The modeling results are sampled at the CMA stations.

1285
1286
1287
1288
1289
1290
1291
1292
1293
1294
1295
1296
1297
1298
1299

1300

1301

1302

1303

1304

1305

1306
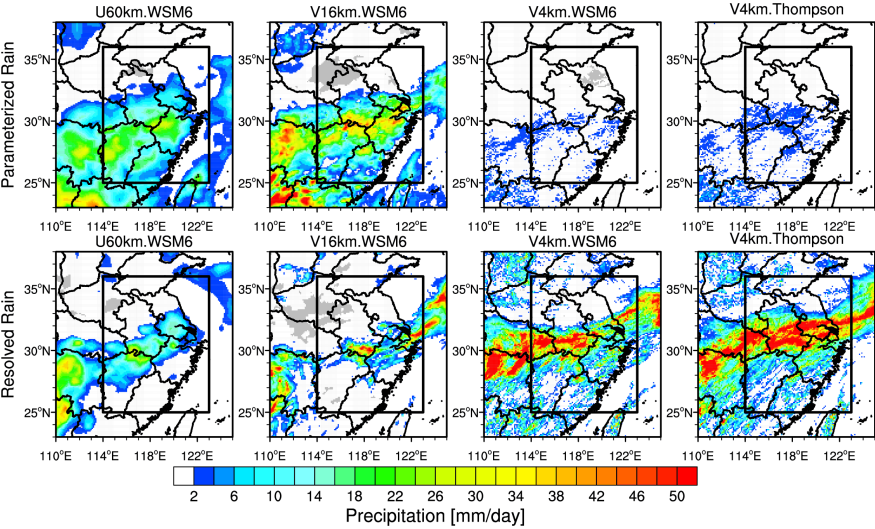
1307

Figure 5 Spatial distribution of averaged parameterized and resolved precipitation during the
event over East China from the simulations with the resolutions of 60 km, 16 km, and 4 km.

1310

1311

1312

1313

1314

1315

1316

1317

1318

1319

1320

41

1321
1322
1323
1324
1325
1326
1327
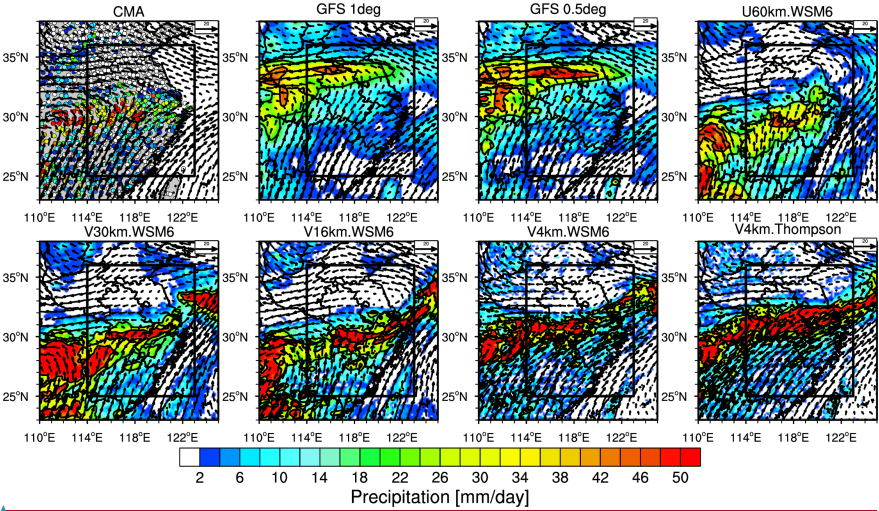
Figure 6 Spatial distributions of precipitation and wind fields at 850 hPa averaged during the event from the MPAS simulations at the resolutions of 60 km, 30 km, 16 km, and 4 km. The observed mean precipitation from the CMA stations and the wind fields from the ERA5 reanalysis are shown as well. The black contour lines represent the precipitation larger than 20 mm/day. The black box denotes the region of East China (25°N-36°N, 114°E-123°E) for the analysis in the following. For comparison, the GFS forecasts at 1 degree and 0.5 degree resolutions are also shown.

1328
1329
1330
1331
1332
1333
1334
1335
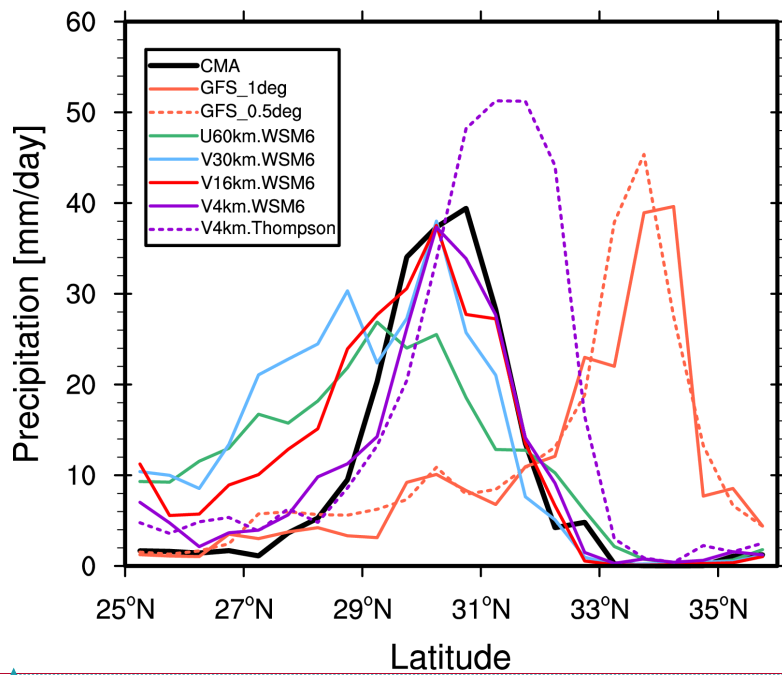1336
1337
1338
1339
1340
1341

Figure 7 Zonal distributions of precipitation averaged during the event averaged over East China (denoted as the black box in Fig. 6) from the CMA station observations and the simulations with the resolutions of 60 km, 30 km, 16 km, and 4 km. For comparison, the GFS forecasts at 1 degree and 0.5 degree resolutions are also included. The modeling results are sampled at the CMA stations.
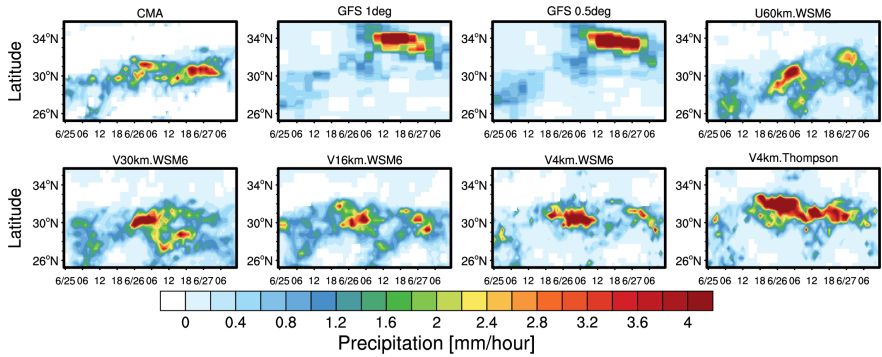
1364

1365

1366

1367

1368

1369

1370

Figure 8 Time-Latitude cross section of precipitation during the event <u>averaged</u> over East China <u>(denoted as the black box in Fig. 6)</u> from the CMA station observations, GFS forecasts at 0.5° and 1.0° resolutions, and the MPAS simulations at resolutions of 60 km, 30 km, 16 km, and 4 km over East China. The simulations at 4 km are with two cloud microphysics schemes (WSM6 and Thompson). The modeling results are sampled at the CMA stations.
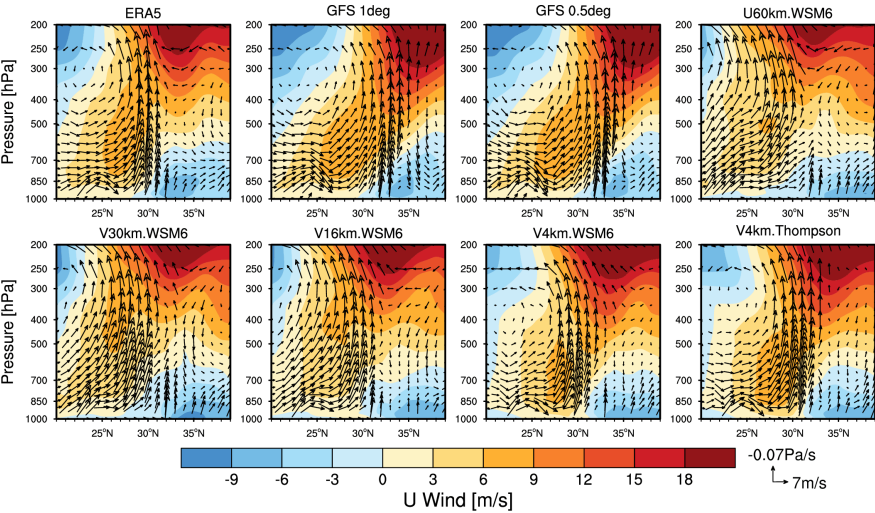
1376

1377

1378

1379

1380

1381

1382

1383

1384

1385

1386

1387

1388

1389
1390
1391
1392
1393
1394
1395
1396

1397
1398
1399
1400
1401
1402
1403

Figure 9 Height-Latitude cross section of wind fields averaged over the region (the entire domain as shown in Fig. 6) during the event from the ERA-interim reanalysis, the GFS forecasts at 0.5° and 1.0° resolutions, and the MPAS simulations at resolutions of 60 km, 30 km, 16 km, and 4 km. The simulations at 4 km are with two cloud microphysics schemes (WSM6 and Thompson). The positive color represents eastward wind. All the datasets are regridded into 0.25° horizontal resolution.

Deleted: as

1404
1405
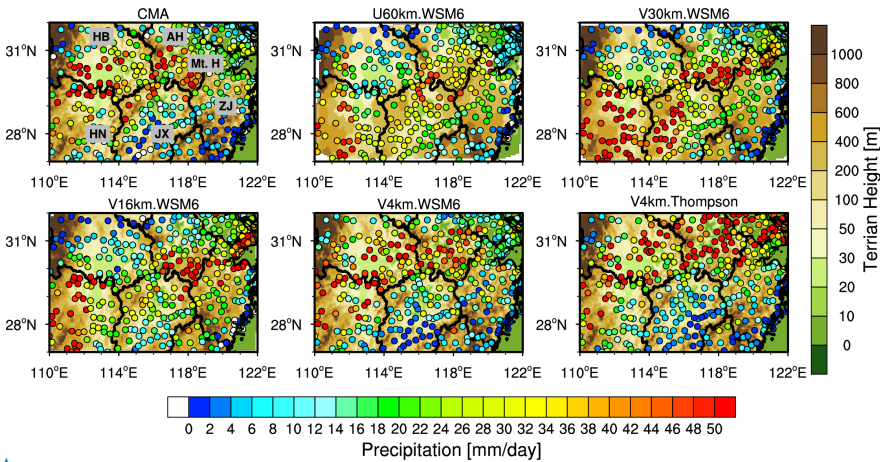1406
1407
1408
1409

1411

1412

1413

1414

1415

1416

Figure 10 Spatial distributions of precipitation averaged during the event over the heavy precipitation region (27°N-32°N and 110°E-122°E) from the CMA observations and the MPAS simulations at the resolutions of 60 km, 30 km, 16 km, and 4 km. The simulations are sampled at the CMA stations. The topography is also shown. In the panel of CMA result, "AH", "ZJ", "HB", "HN", "JX", and "Mt. H" denote the provinces of Anhui, Zhejiang, Hubei, Hunan, and Jiangxi, and Mountain Huang, respectively.
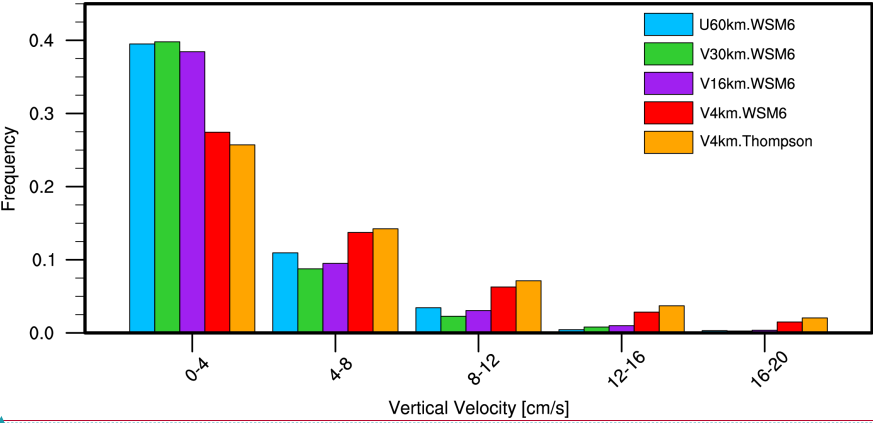
1423

1424

1425

1426

1427

1428

1429

1430

1431

1432

1433

46
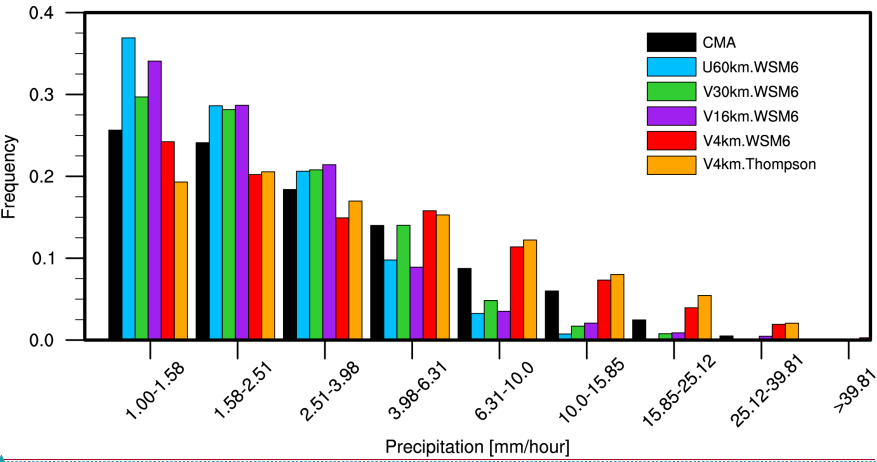
1440
1441
1442
1443
1444
1445
1446
1447
1448
1449
1450
1451
1452
1453
1454
1455
1456
1457
1458

Figure 11 Probability density functions (PDFs) of hourly precipitation at all the CMA stations during the event over East China (denoted as the black box in Fig. 6) from the CMA observations and the MPAS simulations at the resolutions of 60 km, 30 km, 16 km, and 4 km. The simulations are sampled at the CMA stations.
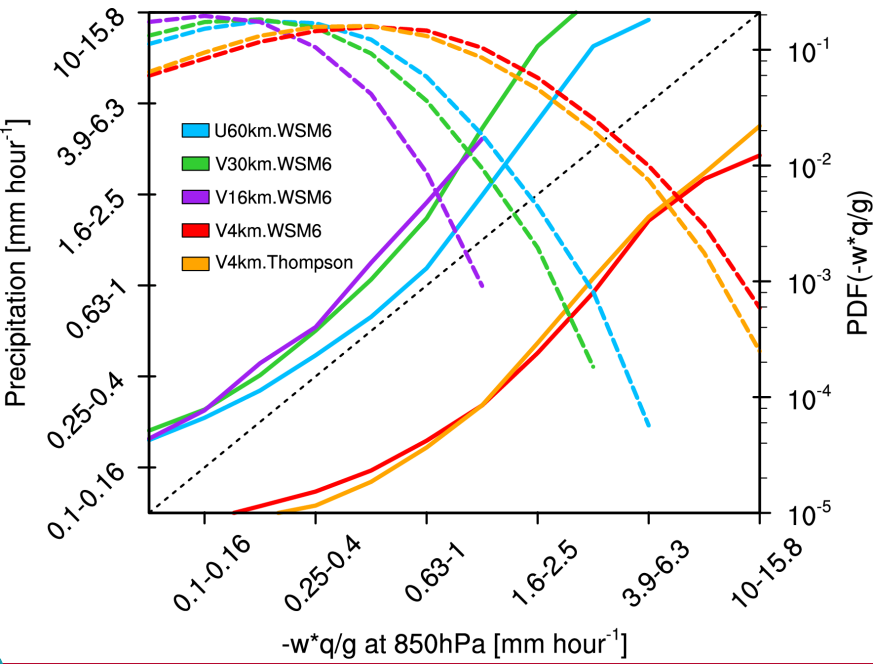
Formatted: Font:(Default) Times New Roman

1459
1460
1461
1462
1463
1464

Figure 12 **Figure 12** Probability density functions (PDFs) of hourly upward vertical velocity averaged below 700 hPa at all the CMA stations during the event over East China (denoted as the black box in Fig. 6) from the MPAS simulations at the resolutions of 60 km, 30 km, 16 km, and 4 km.

1466
1467
1468
1469
1470
1471
1472
1473
1474
1475
1476
1477
1478
1479
1480
1481
1482

Figure 13 Hourly precipitation versus upward moisture flux at 850hPa during the event over East China (denoted as the black box in Fig. 6) from the MPAS simulations at the resolution of 60km, 30km, 16km and 4km (solid line, left axis), and the PDFs of the upward moisture flux (dash line, right axis).

1488
1489
1490
1491
1492
1493
1494

Formatted: Font:(Default) Times New Roman

Table 3 The mean bias (MB) and root mean square root (RMSE) of the simulated results shown in Fig. 6-10 against CMA observations

	GFS.1deg		GFS.0.5deg		U60km.WSM6		V30km.WSM6		V16km.WSM6		V4km.WSM6		V4km.Thompson	
	RMSE	MB	RMSE	MB	RMSE	MB	RMSE	MB	RMSE	MB	RMSE	MB	RMSE	MB
Fig.6 [mm/day]	18.48	1.08	19.62	1.65	14.98	1.99	18.83	5.11	16.80	3.81	14.17	0.59	17.57	3.70
Fig.7 [mm/day]	18.10	0.70	18.79	1.73	9.67	2.18	10.10	3.70	6.31	2.56	3.34	0.31	13.61	5.50
Fig.8 [mm/hour]	1.17	0.06	1.21	0.10	0.78	0.12	0.86	0.18	0.74	0.14	0.83	0.04	1.22	0.26
Fig.10 [mm/day]					21.98	-0.49	28.13	7.43	24.27	3.74	21.25	2.28	25.66	6.48

Page 43: [3] Deleted   **chun zhao**   **5/31/19 8:40:00 AM**

Page 46: [4] Deleted   **chun zhao**   **5/28/19 3:13:00 PM**